Balance between protective and pathogenic immune responses to pneumonia in the neonatal lung enforced by gut microbiota.

Authors: Joseph Stevens[1,2], Shelby Steinmeyer[3,6], Madeline Bonfield[1], Timothy Wang[3,6], Jerilyn Gray[3], Ian Lewkowich[4,6], Yan Xu[3,5,6], Yina Du[3], Minzhe Guo[3,5,6], James L. Wynn[10], William Zacharias[3,6], Nathan Salomonis[5,6], Lisa Miller[7,9], Claire Chougnet[4,6], Dennis Hartigan O'Connor[8,9], and Hitesh Deshmukh[3,4,6]*.

Affiliations:
[1]Immunology Graduate Program, University of Cincinnati, College of Medicine.
[2]Medical Scientist Training Program, University of Cincinnati, College of Medicine.
[3]Division of Neonatology, Cincinnati Children's Hospital Medical Center.
[4]Division of Immunobiology, Cincinnati Children's Hospital Medical Center.
[5]Division of Bioinformatics, Cincinnati Children's Hospital Medical Center.
[6]Department of Pediatrics, University of Cincinnati, College of Medicine.
[7]Department of Anatomy, Physiology, and Cell Biology, University of California, School of Veterinary Medicine, Davis.
[8]Department of Medical Microbiology and Immunology, University of California, School of Medicine, Davis.
[9]California National Primate Research Center, Davis.
[10]Department of Pediatrics, University of Florida, College of Medicine.

* Corresponding Author:
Hitesh Deshmukh M.D., Ph.D.
Cincinnati Children's Hospital Medical Center
3333 Burnet Avenue
Cincinnati, OH 45219
Phone: (513) 803-7448
Email: hitesh.deshmukh@cchmc.org

One sentence summary: Gut microbiota promote clinical recovery by reinforcing the balance between regenerative pathways driving tissue homeostasis and inflammatory responses limiting pathogens in infected neonatal lungs.

Abstract:

While modern clinical practices like cesarean sections and perinatal antibiotics have improved infant survival, treatment with broad-spectrum antibiotics alters intestinal microbiota and causes dysbiosis. Infants exposed to perinatal antibiotics have an increased likelihood of life-threatening infections, including pneumonia. Here, we investigated how gut microbiota sculpt pulmonary immune responses, promoting recovery and resolution of infection in newborn rhesus macaques. Early-life antibiotic exposure, mirroring current clinical practices, interrupted the maturation of intestinal commensal bacteria and disrupted the developmental trajectory of the pulmonary immune system as assessed by single-cell proteomic and transcriptomic analyses of the pulmonary immune response. Early-life antibiotic exposure rendered newborn macaques susceptible to bacterial pneumonia, mediated by profound changes in neutrophil senescence, inflammatory signaling, and macrophage dysfunction. Pathogenic reprogramming of pulmonary immunity was reflected by a hyperinflammatory signature in all pulmonary immune cell subsets. Distinct patterns of immunoparalysis, including dysregulated antigen presentation in alveolar macrophages, impaired costimulatory function in T helper cells, and dysfunctional cytotoxic responses in natural killer (NK) cells, were coupled with a global loss of tissue-protective, homeostatic pathways in lungs of dysbiotic newborns. Fecal microbiota transfer corrected the broad immune maladaptations and protected against severe pneumonia. These data demonstrate the importance of intestinal microbiota in programming pulmonary immunity. Gut microbiota promote balance between pathways driving tissue repair and inflammatory responses, thereby leading to clinical recovery from infection in infants.

Main Text

INTRODUCTION: Distinct immune responses adapted for early postnatal life also render newborns more vulnerable to infections (*1*). Incomplete understanding of immune development early in life contributes to our inability to reduce neonatal morbidity caused by respiratory infection, which unfortunately kills more newborns than any other cause. While a series of coordinated events control the development of the newborn immune system (*2*), few are as important as the interactions of immune cells with successive waves of commensal bacteria that colonize the newborn's intestine after birth (*3, 4*). Evolving microbial signals play a critical role in the maturation of neutrophils, T helper cells, monocytes, and innate lymphoid cells in the peripheral blood and the intestine (*5, 6*). Nevertheless, the role of intestinal commensal bacteria in functional programming of effector immune cells at extra-intestinal mucosal sites, for example, the lungs is unclear (*7*).

A significant proportion of infants are exposed to antibiotics as a routine part of the birthing process(*8, 9*). Infants delivered by cesarean section are exposed to perinatal antibiotics as part of perioperative prophylaxis given to the mothers. Nearly half of vaginally delivered infants are exposed to antibiotics given to the mother to prevent group B streptococcus sepsis (*10-12*). Many of these infants continue to receive empiric antibiotics after birth. While current clinical practices are essential for reducing infant mortality, they may extract a significant biological cost in long-term disruption of the gut microbiota. Infants treated with antibiotics experience more significant morbidity in response to sepsis and pneumonia, (*13-17*) compared to milder disease and spontaneous resolution in infants not exposed to antibiotics.

In the present study, we define how gut microbiota sculpt immune responses that mediate recovery and resolution rather than severe disease. Such an understanding is vital to develop effective treatments for respiratory infections in this vulnerable population. Non-human primate lung more closely resembles human infant lung in structure, developmental stage, physiology, and mucosal immune mechanisms (*18*), compared to the murine lungs (*19*). In addition, like humans, non-human primates develop lobar pneumonia and demonstrate a heterogeneous clinical response (*20*). Their

larger size and similarity to human newborns enable integration of clinical signs, longitudinal assessment of disease progression, and the ability to distinguish mild, self-resolving pneumonia from severe, often fatal pneumonia.

Here, we define a tiered immunologic development program, anchored by stepwise engagement of effector cells to limit tissue damage and promote recovery, that was experimentally disrupted by early-life antibiotic exposure. Remodeling of the pulmonary immune response was anchored by the appearance of a population of senescent, hyperinflammatory neutrophils, dysregulated antigen presentation in macrophages, impaired costimulatory function in T cells, and a dysfunctional cytotoxic response in natural killer (NK) cells. This was all coupled with global loss of tissue-protective, homeostatic pathways in dysbiotic newborns. Fecal microbiota transfer corrected the broad immune maladaptations and protected against severe pneumonia in dysbiotic newborn macaques. Our data suggest that gut microbiota reinforce the balance between regenerative pathways driving tissue homeostasis and inflammatory responses, thereby limiting pathogenesis and promoting clinical recovery. Furthermore, our results highlight a potential role for microbiota transfer as immune support in these 'at risk' infants.

RESULTS:

Antibiotic exposure during the first postnatal week delays microbiota maturation and is associated with pro-inflammatory signatures in the peripheral blood: We treated a cohort of vaginally delivered, nursery raised rhesus macaques (**Supplemental Table 1**) with a cocktail of antimicrobials from postnatal days (PN) 1 to 7 or with saline (n = 4 in each experimental group) (**Fig. 1a**) and profiled the fecal bacterial communities daily. Stools in saline-treated newborn macaques, referred hereafter as control newborns, were dominated by facultative aerobic *Enterobacteriaceae* during the first week of life before changing to strict anaerobes, principally *Bifidobacterium, Bacteroides*, and *Clostridium* (**Fig. 1b, Supplemental Table 2**) in the second week of life, similar to the pattern seen in human neonates (*21, 22*). Dynamic changes in the abundance of peripheral blood neutrophils, $CD4^+$ and $CD8^+$ T helper cells, NK cells, and migratory cytokines occurred contemporaneously with changes in the stool microbiota (**Fig. 1c-e, Supplemental Fig.**

1a-c, Supplemental Table 3 and 4). Temporally restricted patterns of linked changes in immune cell frequencies, abundance of plasma cytokines, and commensal colonization revealed a 'postnatal immune adaptation' signature (**Fig. 1b, d and e, Supplemental Fig. 1e**).

Antibiotic use significantly diminished the abundance of *Enterobacteriaceae,* disrupted the appearance of *Bacteroides* and *Bifidobacterium* during the second week of life, reduced phylogenetic diversity, delayed the maturation of intestinal microbiota (**Fig. 1b and c, Supplemental Table 2 and 5**), creating a maladapted immune state characterized by a pro-inflammatory signature (**Fig. 1e, Supplemental Fig. 1f, Supplemental Table 6).** Frequency and the absolute number of peripheral blood neutrophils, critical for a newborn's defense against pathogens, were decreased in antibiotic-exposed newborn macaques, referred hereafter as dysbiotic newborns (**Fig. 1d, Supplemental Fig. 1d)**. Neutrophils in dysbiotic newborns were phenotypically distinct, marked by increased expression of CD11b, a marker for neutrophil activation (*23*) and programmed death (PD-1), a marker associated with senescence/exhaustion (*24, 25*) (**Fig. 1f and g**). CD45RA, CD38, and CD57, markers associated with T cell differentiation (*26*) and senescence (*27-30*), respectively, were co-expressed at higher levels in $CD4^+$ T helper cells from dysbiotic newborns (**Fig. 1f and g**).

Gene networks associated with 'cellular stress', 'inflammation', and 'ubiquitination and apoptosis' were abundant in the transcriptomic analysis of peripheral blood from dysbiotic newborns (**Supplementary Table 6**). Collectively, these data demonstrate that disruption of commensal microbes by early-life antibiotic use causes a maladapted state marked by both a robust, pro-inflammatory bias and neutrophil and T cell exhaustion.

Early-life antibiotic exposure is associated with clinically severe pneumonia. After discontinuing antibiotics for one week, we challenged the newborn macaques in each experimental group with *S. pneumoniae* (serotype 19F), a common and often fatal respiratory pathogen in human infants (*31*). Vital signs, including heart rate, respiratory effort, blood pressure, urine output, oxygen saturation, and overall clinical condition of these newborn macaques, were monitored every 6 hours. In addition, chest radiographs were obtained daily. The pediatric early warning score (PEWS) (*32*), an extensively

validated clinical decision-making and severity-scoring tool, was used to guide therapy, including intravenous fluids and supplemental oxygen (**Supplemental table 7**). Thus, we provided these newborn macaques with intensive care comparable to what a human infant with pneumonia would receive, with the exception of additional antibiotics after challenge with *S. pneumoniae*.

The clinical status of dysbiotic newborns deteriorated, evidenced by higher peak PEWS score and radiographic evidence of consolidation (**Fig. 1h and j**). The progression of symptoms was also more rapid in the dysbiotic newborns (**Fig. 1i**). The majority required supportive therapy, an objective measure of clinical well-being. Almost all dysbiotic newborns received supportive treatment by 60 hours (**Fig. 1k**, **Supplemental table 7**), recapitulating the rapid progression and increased morbidity seen in dysbiotic human infants (*33-35*). These data together demonstrate that this newborn macaque model mirrors a clinically relevant disease process and allows for profiling of the immune response in target tissues, such as lungs, which is often impossible in human newborns.

Early-life antibiotic exposure remodels pulmonary immune responses to *S. pneumoniae* infection. The host inflammatory response to pneumonia is highly compartmentalized in the lungs (*36*), so systemic immune cell or cytokine responses alone may not thoroughly explain the differential clinical response to pneumonia in dysbiotic newborns. We, therefore, used a combination of single-cell RNA-sequencing (scRNAseq) and high-parameter (>20 markers) CyTOF to then profile both innate and adaptive immune cell responses in the lungs of control or dysbiotic newborns 60 hours. after infection with *S. pneumoniae*. At this time, dysbiotic newborns had more severe disease (PEWS = 8 ± 1.5) than control newborns (PEWS = 5 ± 0.6), despite similar pathogen burden in the lungs **(Supplemental Fig. 1g and h**).

Cell clusters identified in the pulmonary tissues after infection with *S. pneumoniae* in control or dysbiotic newborns were annotated using signature genes from published scRNAseq atlases (*37*)·(*38*) (**Fig. 2a and b, Supplemental Table 8**). The proportion of neutrophils identified by scRNAseq decreased in dysbiotic newborns, whereas the T cell proportion increased (**Fig. 2c and d**). This mirrors the high-parameter CyTOF

cytometry where the frequency of neutrophils decreased approximately 40% in the lungs of dysbiotic newborns, compared to control newborns after infection with *S. pneumoniae* (**Fig. 2e and f, Supplemental Fig. 2a-c**). In contrast, the frequency of $CD4^+$ T cells expanded 2-fold in the lungs of dysbiotic newborns after infection with *S. pneumoniae* (**Fig. 2e and f, Supplemental Fig. 2a-c**). Proportions of other immune cells, for example, alveolar (AM) and interstitial (IM) macrophages, NK cells, B cells, and dendritic cells (DC) subsets, were generally unchanged.

Canonical immune programs anchored by cell migration, differentiation, activation, and tissue repair were broadly disrupted in the pulmonary immune cells of dysbiotic newborns after infection (**Fig. 2g, Supplemental Fig. 2d**). Conversely, immune programs dominated by inflammation (NF-κB activity, IL-1β activation, and glycolysis) and dysfunction (apoptosis, cellular stress, and ubiquitination) were active in all pulmonary immune cells of dysbiotic newborns (**Fig. 2g, Supplementary Table 9**). Furthermore, consistent with transcriptomic changes, cytokines associated with inflammation (CXCL8, CXCL10, and TGFβ) and activation (IL6, IL8, and TNF-α) were increased. In contrast, cytokines associated with tissue repair (GMCSF, IL10, and PDGF) were decreased in the bronchial lavage fluid of dysbiotic newborns, with these cytokine levels correlating with disease severity (**Supplemental Fig. 2e and f, Supplemental Table 10**).

Neutrophils, AMs, and, to a lesser extent, IMs, were the principal sources of inflammatory cytokines after infection with *S. pneumoniae* (**Supplemental Fig. 2g)**, consistent with their critical roles in lung defense against pneumonia. Neutrophils and AMs also exhibited the greatest transcriptomic remodeling (**Fig. 2h**) and most differentially expressed transcripts related to inflammation and tissue repair (**Fig. 2i, Supplemental Fig. 2d and g**) in dysbiotic newborn macaques after infection with *S. pneumoniae*. A similar reconfiguration of immune responses was associated with rapid disease progression, worse symptoms, and increased mortality in humans in both bacterial and viral (influenza and SARS-Cov2) pneumonia (*39-44*).

Senescent and hyperinflammatory neutrophils dominate pulmonary immune responses to *S. pneumoniae* infection in dysbiotic newborns. We identified three transcriptionally distinct neutrophil populations in the lungs after infection with *S.*

pneumoniae (**Fig. 3a and b**, **Supplemental Fig. 3a**, **Supplemental Table 11**). Neutrophil heterogeneity is influenced by developmentally-encoded cell programs and by environment and pathogen-specific factors (*45*). To identify distinct neutrophil populations, we used module scores (*38*), reflecting the average expression of all genes related to neutrophil development, maturation, and activation using published gene signatures from granulocytes during homeostasis and in the setting of sepsis (*46*) (**Supplemental Table 12**). The population identified by expression of genes related to 'pathogen response' and 'cytokine signaling' reflected neutrophil heterogeneity caused by pathogen exposure (**Fig. 3b and c, Supplemental Fig. 3a**) represents mature neutrophils (cluster 1). Neutrophils characterized by high expression of *CXCR4* and *CD63* and reduced expression of *CXCR2* and *SELL* (**Fig. 3b and c, Supplemental Fig. 3b**) represent stressed, hyperinflammatory neutrophils (*47*) (cluster 2). These cells also had increased gene transcripts associated with glycolysis, a pathway associated with hyperinflammatory responses (*48*) (**Supplemental Fig. 3b and c**). Immature neutrophils (cluster 3) were identified based on expression of gene transcripts related to neutrophil maturation (secretory vesicles, lysozymes, and phagocytosis) (**Fig. 3b and c, Supplemental Fig. 3b**). The developmental relationship among these three clusters was predicted by cellular trajectory analysis (*49-52*) (**Fig. 3d**). Pseudotime analysis of granule proteins, *OLFM4* and *SELL*, and trafficking receptors, *CXCR2* and *CXCR4*, known to be involved in neutrophil maturation, supported a continuum of differentiation from immature neutrophils (cluster 3) to mature neutrophils (cluster 1) to senescent, hyperinflammatory neutrophils (cluster 2) (**Fig. 3e**).

Early-life antibiotic exposure strongly influenced the activation state of the lung neutrophil compartment after infection with *S. pneumoniae.* Pseudobulk RNAseq analysis of these pulmonary neutrophils identified distinct signatures associated with dysbiosis (**Supplemental Fig. 3c**). Senescent, hyperinflammatory neutrophils were unique to the lungs of dysbiotic newborns, while mature neutrophils were absent in the lungs of dysbiotic newborns (**Fig. 3f**). CyTOF then also showed a consistent remodeling of the pulmonary neutrophil pool with the emergence of stressed, senescent ($CXCR2^{lo}$, $CXCR4^{hi}$, $CD62L^{lo}$) neutrophils in the lungs of dysbiotic newborns after infection with *S. pneumoniae* (**Fig. 3g and h**).

There was broad induction of NFκB (a pro-inflammatory cytokine-encoding gene regulator), enrichment of phagocytosis and degranulation gene sets, and increased expression of epigenetic regulators associated with inflammatory neutrophils, including *PADI4*, which is required for NETosis (*53, 54*) and *CD274* (encoding for PD-L1 (*55*)), a marker of cell exhaustion in pulmonary neutrophils from dysbiotic newborns (**Supplemental Table 13**). We noted consistent changes in neutrophil activating and chemotactic cytokines in the bronchial washings of dysbiotic newborns after infection with *S. pneumoniae* (**Supplemental Fig. 3d**).

Remodeled pulmonary neutrophil compartment is associated with increased pneumonia-related morbidity in dysbiotic newborns. Dysfunctional neutrophils contribute to pulmonary damage in experimental models of acute lung injury (*56, 57*)(*58*). Conversely, neutrophil depletion is protective in several pneumonia models, and severe disease is frequently associated with an increased pulmonary neutrophil influx. We therefore hypothesized that these dysfunctional, senescent neutrophils contributed to severe pneumonia in dysbiotic newborns. We identified the five most differentially-expressed genes between senescent, hyperinflammatory neutrophils and all other cells in our dataset: *HIF1A, CXCR4, CD274, LTF*, and *S100A8*. We then used publicly available whole-blood bulk transcriptomic datasets of infants and children with severe sepsis and pneumonia (*59*). We scored each sample in these datasets by the aggregated expression of these five genes. We used these scores to construct a receiver operating characteristic (ROC) curve using the gene score as a predictor and severity as the response variable. Our senescent, hyperinflammatory neutrophil gene score predicted mortality and disease severity (AUC = 0.79) in infants with severe sepsis and pneumonia (**Fig. 3i, Supplemental Fig. 3e, Supplemental Table 14**). Our data suggest that significant remodeling of the lung neutrophil compartment, anchored by the emergence of senescent and hyperinflammatory neutrophils, contributes to increased pneumonia-related morbidity in dysbiotic newborns. The gene signatures from these senescent and hyperinflammatory neutrophils are potential prognostic indicators in human infants with sepsis and pneumonia.

Predicted regulatory networks active in pulmonary neutrophils from dysbiotic newborns after infection with *S. pneumoniae*. Regulatory networks anchored by the

transcription factors C/EBPγ (encoded by *CEBPG*) and Kruppel-like factor (KLF) 6, which are essential for neutrophil development (*60-65*), were enriched in immature neutrophils (cluster 3) (**Fig. 3j, Supplemental Table 15**). Regulatory networks anchored by defense response-associated transcription factors (*66-68*), for example, NFKB, IRF7, STAT5A, BATF3, and HIF1A, were enriched in activated neutrophils (cluster 1) (**Fig. 3j and k, Supplemental Table 15**). In contrast, regulatory networks anchored by epigenome modifying enzymes (*69*), lysine demethylase KDM5A, histone deacetylase HDAC2, and nuclear factor interleukin 3 (NFIL3), a component of the circadian clock, were enriched in senescent, hyperinflammatory neutrophils (cluster 2) (**Fig. 3j and k, Supplemental Table 15**). NFIL3 and KDM5A are implicated in the microbiota-driven regulation of both nonhematopoietic cells, such as the intestinal epithelium, and hematopoietic cells, such as ILCs and NK cells, by chromatin histone modification (*70-73*). Disruption of NFIL3 and KDM5A regulatory pathways may explain neutrophil dysfunction in dysbiotic newborns and highlights the need for experimental validation of their role in neutrophil homeostasis.

Macrophages with dysfunctional features are a hallmark of the remodeled pulmonary immune response in the dysbiotic macaques. To interrogate macrophage plasticity, which is informed by developmental programs and tissue and stress-specific signals (*74-76*), we used MacSpectrum*(77)*, an analytical tool to stratify macrophage maturation and activation. The dominant population enriched for gene transcripts associated with 'antigen processing and presentation' represents terminally differentiated mature AM (cluster 1) (**Fig. 4a-e**). The population enriched for transcripts associated with 'inflammation', 'purinergic-inflammasome signaling' and 'IL1 receptor activation' was identified as polarized, inflammatory AMs (cluster 2) (**Fig. 4a-e**). Immature AMs were identified based on expression of gene transcripts associated with 'DNA replication and cell division' (cluster 3) **(Fig. 4a-e, Supplemental Table 16**). Cellular trajectory analysis identified a relationship between differentiation and activation as the AM developed from immature (cluster 3) to mature (cluster 1) to polarized inflammatory AM (cluster 2) (**Fig. 4f**).

Early-life antibiotic exposure strongly influenced the development and activation state of AMs after infection with *S. pneumoniae.* Mature AMs (cluster 1), known to maintain noninflammatory states by promoting tolerance and facilitating tissue repair (*78*), were decreased in dysbiotic newborns. In contrast, the frequency of polarized, inflammatory AMs (cluster 2) was increased also in dysbiotic newborn macaques (**Fig. 4g**). Also, CyTOF cytometry demonstrated that the frequency of M1-activated AMs (identified as live $MHCII^+$, $CD11C^+$, $CD11B^+$, $CD86^+$ cells) was increased in dysbiotic newborns after infection with *S. pneumoniae,* consistent with scRNAseq findings (**Fig. 4h**), and correlated with disease severity (**Supplemental Fig. 4i**).

We hypothesized that dysfunctional inflammatory macrophages were associated with severe pneumonia in dysbiotic macaques. Using published gene signatures from AMs in acute respiratory distress syndrome (ARDS) in humans (*46*), we found that gene transcripts predicting recovery were enriched in cluster 1 (**Fig. 4i, Supplemental Table 17**). Conversely, gene transcripts predicting severe ARDS/death were enriched in cluster 2 (**Fig. 4i, Supplemental Table 17**). Consistent with our hypothesis, expression of genes related to tissue damage and vascular inflammation were differentially enriched in dysbiotic macaques (**Fig. 4j and Supplemental Table 18**). ATP released from damaged epithelium and endothelium activates an ATP-driven purinergic-inflammasome signaling pathway and is associated with fatal pneumonia and severe ARDS (*79*). Consistent with the above observations, we found increased ATP levels in the bronchial lavage fluid of dysbiotic macaques that did not reach statistical significance ($p = 0.06$) (**Supplemental Fig. 4g**). Finally, decreased expression of tolerance promoting MHC class II genes further supports the global dysfunction of AM in dysbiotic newborns (**Fig. 4j**).

Antibiotic exposure also remodeled the IM pool after infection with *S. pneumoniae.* Analogous to AM, we identified three unique populations of mature IM marked by expression of genes related to macrophage migration, phagocytosis, tolerance promotion, and wound repair (Cluster 1); activated IMs identified by their expression of genes related to antigen presentation, IL1 receptor activation, and T helper cell differentiation (Cluster 2); and a population marked by expression of genes associated with ER stress, exhaustion, and apoptotic clearing, identified as exhausted and stressed IM (Cluster 3) (**Supplemental Fig. 4a-d**). In addition, antibiotic exposure was associated with contraction of pro-repair IMs and expansion of stressed, exhausted pro-inflammatory

IMs (**Supplemental Fig. 4e, f, h, and i, Supplemental Table 19**). Collectively, these data suggest that the loss of pro-phagocytic, tolerance-promoting, and antigen-presentation programs, which facilitate protective functions of lung macrophages and expansion of ATP-purinergic inflammasome signaling and pro-inflammatory programs are associated with lung damage and increased pneumonia-related morbidity in dysbiotic macaques.

Conserved gene regulatory networks are associated with remodeled pulmonary neutrophil and macrophage compartments in dysbiotic newborns. Regulatory networks anchored by PPARγ (encoded by *PPARG*), C/EBPα (encoded by *CEPBA*), PU.1 (encoded by *SPI1*) (*80*), and USF1, TFs critical in macrophage development(*81*), were enriched in all mature AMs (**Fig. 4k and l, Supplemental Table 20**). HIF1A and EGR, critical drivers of transcriptional programs underlying macrophage activation and terminal polarization(*82*), were more enriched in stressed and hyperinflammatory macrophages (**Fig. 4k and l, Supplemental Table 20**).

A regulatory network anchored by ARNTL (encoded by *BMAL1*), a component of the circadian clock, was uniquely overrepresented in the stressed and hyperinflammatory macrophages (cluster 2) that was expanded in dysbiotic newborns (**Fig. 4k and l**). Diurnal oscillations of intestinal microbiota are thought to drive the programming of host immune responses via ARNTL (*83*) and other components of the circadian clock. In addition, RXRA and NFIL3 were overrepresented in regulatory networks for cluster 2 (**Fig. 4k**). These data, coupled with similar observations in neutrophils (**Fig. 3j and k**), suggest a role for shared regulatory networks anchored by circadian clock components in the transcriptional remodeling of pulmonary neutrophil and alveolar macrophage compartments in dysbiotic newborns.

Ineffective pulmonary T helper cell responses in dysbiotic newborns after infection with *S. pneumoniae*. In contrast to the significant remodeling of the myeloid compartment, we observed more modest changes in the distribution of various pulmonary T cells between dysbiotic and control newborns (**Supplemental Fig. 5a-c**). Cytokines associated with T cell differentiation and effector responses, such as IL6, IL8, IL17, CXCL8, and CXCL10, increased in the bronchial lavage fluid of dysbiotic macaques (**Supplemental Fig. 2d, Supplemental Fig. 5d**). Hyper- or hypoactivation of T cells, or

skewing towards an ineffective differentiation state, such as T_H17 cells, exhausted T cells, or terminally differentiated T cells, are associated with severe viral pneumonia in animal models (*84*). The majority of pulmonary T helper cells from dysbiotic newborns co-expressed CD279 (PD-1) and CD38, markers linked to T cell exhaustion (*85-88*), and showed decreased expression of costimulatory molecules, CD28 and CD40 (**Supplemental Fig. 5e**). The frequency of dysfunctional $CD4^+$ T helper cells (co-expressing CD279 and CD38) correlated with disease severity (**Supplemental Fig. 5f**).

We noted decreased gene transcripts related to 'tissue repair and growth factor signaling', 'T cell fitness', and 'effector differentiation' in T cells from dysbiotic newborns (**Supplemental Fig. 5g, Supplemental Table 21)**. Transcripts for genes in the aerobic glycolysis pathway, linked to T cell exhaustion (*89, 90*), were increased in T cells of dysbiotic newborns (**Supplemental Fig. 5g, Supplemental Table 21**). Our data suggest that inappropriate T cell responses, marked by a failure to limit 'cytotoxicity' and increased tendency towards 'exhaustion', dominate immune response in dysbiotic newborns and contribute to tissue damage and increased morbidity, perhaps consistent with recent studies highlighting the critical role of exhausted T cells in severe COVID-19 illness (*86, 91-93*).

Early-life antibiotic exposure increased stressed, inflammatory NK cells in lungs of dysbiotic newborns after infection with *S. pneumoniae*. Optimal NK cell functions promote infection control by serving as a rheostat in regulating T cell responses, and excessive activation contributes to immunopathology (*94*). Consistent with these observations, we found that most NK cells in the lungs of dysbiotic newborns co-expressed activation marker CD69 and produced granzyme B and IFNγ, identifying them as cytotoxic and stressed NK cells (**Supplemental Fig. 5h**).

Similar remodeling of the pulmonary NK pool was supported by scRNAseq. Expression of cytotoxic effector and activation markers, such as *NKG7*, *CD38*, and *CD52* (*41, 95, 96*), and proliferation markers, such as *MCM*, *PCNA*, and *EIF4A1*, identified $CD56^+$ NK cells (Cluster 2) and proliferating NK cells (Cluster 3), respectively (**Supplemental Fig. 5i and j**). In contrast, a cluster expressing transcripts associated with cell survival, cellular stress, and inflammation represented cytotoxic and stressed NK cells (Cluster 1) (**Supplemental**

Fig. 5i and j). The numbers of cytotoxic and stressed NK cells expanded in dysbiotic newborns, consistent with CyTOF analysis (**Supplemental Fig. 5k**). Next, the transcriptomic analysis further revealed an increased abundance of transcripts associated with T cell activation (*97*), inflammation, and exhaustion in dysbiotic newborns **(Supplemental Fig. 5l, Supplemental Table 22**). These data, coupled with reports implicating dysfunctional cytotoxic NK cell responses in severe COVID-19(*41*), suggest that defects in NK cell cytotoxicity may be associated with adverse outcomes caused by pneumonia in dysbiotic newborns.

Miscommunication between innate and adaptive immune cells uncouples inflammatory and pro-repair pathways and contributes to increased severity of pneumonia in dysbiotic newborns. To identify altered cell-cell communication in the lungs of dysbiotic newborns following infection, we utilized a novel analytical tool, CellChat (*98*), to infer cell signaling interactions based on ligand-receptor transcriptional abundance. Globally, signaling pathways related to chemotactic localization (*99-102*), such as CXCL, CCL, and SELPLG, and tissue homeostasis and repair(*103, 104*), such as NOTCH and SEMA4, were dominant in control newborns (**Fig. 5a and b**). In contrast, signaling pathways related to inflammation(*105, 106*), such as CD86 and RESISTIN, and cell exhaustion(*107, 108*), such as PDL1 and PDL2, were dominant in dysbiotic newborns (**Fig. 5a and b**), suggesting a global rewiring of immune cell-to-cell communication network in dysbiotic newborn macaques (**Fig. 5c, Supplemental Figure 6a-c**).

Dysfunctional macrophages were the 'central hub' of misdirected cell-cell communications (**Fig. 5d and e, Supplemental Fig. 6a and b**). In contrast, neutrophils and, to a lesser extent, T cells were predicted to be 'targets' of such miscommunications, which included immune-inhibitory interactions, such as CD274[PD-L1]-PDCD1, MIF-CD74/CD44/CXCR4, CD86-CD28, and PTPRC-CD22 in dysbiotic newborns (**Fig. 5d and f, Supplemental Fig. 6c-e, g, and i**). These interactions may cause neutrophil and lymphocyte dysfunction. In control newborns, communication circuits between macrophages and neutrophils or T cells were dominated by pathways related to interleukin and chemokine signaling, such as IL1A/B-IL1R2 and CXCL1/3/8-CXCR2, immune co-stimulation and complement activation, such as C3-C3AR1, and tissue repair, such as NOTCH, SEMA4 and THY1 (**Fig. 5d, Supplemental Fig. 6f and h**) (*109, 110*).

These data identify a potential mismatch between inflammatory and pro-repair pathways anchored by dysfunctional macrophages in dysbiotic newborns.

To identify the communication circuits informing the pathogenic remodeling of the pulmonary neutrophil pool, we interrogated specific signaling circuits between AM and neutrophils. AM-derived paracrine signals related to neutrophil migration, such as CXCL-CXCR2 and THBS1-CD47, neutrophil extravasation, such as ITGB2-ICAM1, and neutrophil activation, such as SELPLG-SELL, were enriched in control newborns. In contrast, pathways related to programmed cell death (CD80-CD274[PD-L1]) were dominant in dysbiotic newborns (**Fig. 5e-g, Supplemental Figure 6c-e and 6j)**. PD-L1 negatively regulates the activation of T cell receptors and mediates lymphocyte apoptosis. Severe and often fatal sepsis is marked by increased neutrophil PD-L1 expression(*109, 111*), suggesting a role for PD-L1 in pathogenic responses.

Collectively, these findings highlight the miscommunication between innate and adaptive immune cells in dysbiotic newborns, contributing to a hyperinflammatory signature in neutrophils and relative immune paralysis in the T cells (**Fig. 5h, Supplemental Fig. 6j**). This reinforces the concept that the uncoupling of inflammatory and pro-repair pathways contributes to increased severity of pneumonia in dysbiotic newborns.

Fecal transfer was associated with favorable changes in pulmonary immune cell responses and improved host resistance to pneumonia in dysbiotic newborns. Although no specific bacterial taxa have been consistently associated with pulmonary host resistance to pathogens, fecal microbiota transplantation, which transfers the entire gut microbiota from one host to another, has demonstrated improved clinical outcomes in immunotherapy trials (*110, 112, 113*). We performed fecal transfer (FT); wherein, the fecal contents of control newborns were transferred to dysbiotic newborns on postnatal day 8. Dysbiotic newborns who received fecal transfer, referred hereafter as FT-recipient newborns, were challenged with *S. pneumoniae* on postnatal day 14 (6 days post fecal transfer). FT-recipients had lower PEW score post-infection, less rapid progression of symptoms, and reduced need for supportive therapy (**Fig, 6a-d**). Although all recipients demonstrated clinical benefit, the benefit was variable (**Fig. 6e and f**).

Gut microbiota composition of the FT-recipients (post-treatment) differed from their baseline (pre-FT) (**Fig. 6e**). We observed a non-significant shift of FT-recipients' microbiota toward donor microbiota and those FT-recipients that engrafted closer to the donor displayed a more robust clinical response (**Fig. 6e, Supplemental Table 23**). After FT, gut microbiota had a higher abundance of *Bifidobacterium bifidum*, a favorable modulator of immune responses in humans (*6, 22, 114*) (**Fig. 6g**). The probiotic strain *Bifidobacterium longum* 5^{1A} was associated with a reduced pro-inflammatory response, decreased neutrophil recruitment, and improved ability to combat pulmonary infections induced by *Klebsiella pneumoniae* in mice(*115, 116*). While our study lacked the power to establish a clear association between specific bacterial taxa and clinical response to pneumonia, our results indicate FT could be feasible and potentially effective in restoring host resistance in dysbiotic newborns.

Next, we evaluated the immunological effects of FT after infectious challenge with *S. pneumoniae*. The pulmonary neutrophil pool expanded after FT, although the numbers remained lower than control newborns (**Supplemental Fig. 7a**). Proportions of other immune cells, such as AMs, IMs, NK cells, B cells, platelets, and DC subsets, were generally unchanged after FT (**Supplemental Fig. 7b-c**). FT partially corrected the remodeling of the neutrophil pool observed in dysbiotic newborns (**Fig. 6h**). Numbers of stressed and senescent neutrophils were decreased in lungs of FT-recipients (**Fig. 6h, Supplemental Fig. 7d**). Mature neutrophils, conspicuous by their absence in dysbiotic newborns, reappeared, although their numbers remained lower in control macaques (**Fig. 6h**). FT was associated with changes in the transcriptome of neutrophils compared to dysbiotic macaques. Transcripts of genes related to leukocyte apoptosis, such as *CTSC*, *TRADD*, *PYCARD*, and *C1QBP*, respiratory burst, such as *MPO*, *NCF1*, and *NCF2*, and cellular stress and ubiquitination, such as *HIF1A*, *EGR1*, *NOP53*, and *TANK*, which were previously increased in neutrophils of dysbiotic macaques, were decreased in FT-recipient newborn macaques (**Fig. 6i, Supplemental Fig. 7e, Supplemental Table 24**).

Expression of genes related to inflammasome or IL1-signaling, such as *NLRP3*, *IL1B*, *IL10RA*, and *NFKB1*, decreased in AMs of FT-recipient macaques compared to dysbiotic macaques (**Fig. 6i, Supplemental Fig. 7f, Supplemental Table 25**).

Gene transcripts related to macrophage migration, such as *CCR2*, *CCL3*, *CX3CL1*, phagocytosis, such as *CLEC7A, CD47,* and *C3*, molecules promoting tolerance, such as *CCR2*, *ADA, IL10,* and *FCRL3*, and wound repair, such as *ANG*, *IL10*, and *VEGFA*, remained unchanged in FT-recipients (**Fig. 6i, Supplemental Fig. 7f, Supplemental Table 25**). Transcripts associated with T cell activation and differentiation, such as *IL7R*, *CCR7*, *CD3D*, *CD3E*, and antigen processing and presentation, such as *CCR4*, *ICOS*, and *LYN*, which were severely decreased in T cells of dysbiotic newborns, increased, albeit partially, after FT (**Fig. 6i, Supplemental Fig. 7g, Supplemental Table 26**). Transcripts associated with tissue repair and growth, such as VEGF, PDGFA, and EGF, did not recover (**Fig. 6i, Supplemental Table 26**).

Miscommunication between the innate and adaptive immune cells was reversed after FT (**Supplemental Fig. 7h**). Dysregulated signaling pathways related to inflammation (IL1, IL6, IFN-γ) and immune co-stimulation (CD45) were corrected in FT-recipients **(Fig. 6j)**. However, signaling pathways associated with tissue repair (NOTCH, IL10 and SEMA4) and chemotaxis (CXCL) remained dysregulated in FT-recipients **(Fig. 6j**, **Supplemental Fig. 7h)**. These data suggest that while FT reversed cell stress and apoptosis and mitigated pro-inflammatory signatures in the pulmonary immune cells, it did not fully reverse the loss of innate immune cell migration, differentiation, activation, and tissue repair signatures.

DISCUSSION:

The use of newborn rhesus macaques permitted a highly granular examination of pulmonary and systemic immune responses to a common respiratory pathogen, not possible in either murine or human neonates alone. Their larger size and similarity of lung structure, developmental stages, physiology, and mucosal immune mechanisms (*18*) to human infants, coupled with the longitudinal assessment of disease progression, permitted us to distinguish mild, self-resolving pneumonia from severe pneumonia. In this study, succession of microbial communities in vaginally delivered macaques was similar to the pattern seen in human neonates (*21, 22*), with an abundance of *Gammaproteobacteria* and *Bifidobacterium bifidum,* taxa reported to favorably modulate immune response in humans. Early-life antibiotic exposure disrupted the evolution of

gut microbiota in newborn rhesus macaques. *Bacteroides* and *Parabacteroides* were underrepresented, whereas *Enterococcus* and *Clostridium* were overrepresented, similar to gut microbial communities in a large cohort of vaginally delivered infants exposed to perinatal antibiotics (*117, 118*). This early-life antibiotic exposure was associated with increased morbidity to *S. pneumoniae,* recapitulating epidemiological observations (*33-35*).

We found that early-life antibiotic exposure created a maladapted immune state, characterized by a solid pro-inflammatory signature in the peripheral blood**.** Longitudinal high-dimensional data from next-generation sequencing, plasma proteins, and high-parameter CyTOF provided a further opportunity to integrate diverse data related to individual immune cell populations and plasma proteins in neonates (*119*). However, prior studies were limited to healthy newborns (*120*) and could not assess either rapid changes in the neonate's immune system during the first two weeks of life (*121*) or effects of dysbiosis (*122*). Our present approach revealed heterogeneity in immune ontogeny, converging around neutrophil development and activation, in the first week of life. Developmental changes in T cell migration and maturation were apparent by two weeks of age with adaptations dependent on commensal colonization. Early-life antibiotic exposure created a maladapted immune state, characterized by neutrophil exhaustion and reduced T cell functional capacity, rendering the neonatal macaque susceptible to pneumonia.

Pathogen burden was similar in the lungs of control and dysbiotic newborns, suggesting that the differential clinical response to pneumonia in dysbiotic newborns was unlikely due to inadequate antimicrobial defenses. In contrast, early-life antibiotic exposure remodeled the pulmonary neutrophil compartment by enhancing the presence of senescent neutrophils with an 'exhausted' and 'hyperinflammatory' signatures. A gene signature based on transcriptomic analysis of senescent, hyperinflammatory neutrophils predicted mortality and disease severity in an independent cohort of infants and children with severe sepsis and pneumonia. Hypoxia in the inflammatory microenvironment and bacterial infections, in general, activate pro-survival/anti-apoptotic mechanisms in neutrophils via HIF1A (*123*)- and HIF2A (*124*)-dependent mechanisms. In our study, HIF transcripts were enriched in dysbiotic macaques. We speculate that extended neutrophil

lifespan and the resulting exhaustion, coupled with failure to remove senescent and exhausted neutrophils from the infected lungs, caused severe tissue damage due to the release of proteases, cationic peptides, and cytokines, which were increased in dysbiotic newborn macaques. An extended neutrophil lifespan was observed in patients with sepsis (*125*), ARDS (*126*), severe asthma (*127*), or acute coronary artery disease (*128*) and was associated with disease progression and poor prognosis. Our data suggest that therapeutic approaches targeting hyperinflammation, neutrophil clearance from inflamed tissues, or induction of neutrophil apoptosis may have the potential to improve clinical outcomes in infected, dysbiotic infants.

Early-life antibiotic exposure also remodeled the macrophage pool with contraction of the anti-inflammatory, pro-repair macrophage subset in dysbiotic newborns. Macrophages may be phagocytosing dying/dead epithelial cells and neutrophils, contributing to reduced pathogen burden and decreased tissue damage in control newborn macaques, consistent with their pro-homeostatic role in pathogen control and inflammation resolution (*129*). In contrast, dysbiotic newborn macaques demonstrated a dominance of inflammatory, terminally-polarized macrophages and a trend towards increased ATP levels. Expanded ATP-purinergic-inflammasome signaling is associated with ARDS, fibrosis, and worse clinical outcomes in viral pneumonia, including severe COVID-19 (*42, 130-132*). We speculate that in the absence of pro-phagocytic, tolerance-promoting, antigen-presentation function, the pro-inflammatory program in the macrophage is pathogenically turned on in dysbiotic newborn macaques, contributing to excessive lung damage and increased infection-related morbidity.

Disrupted circadian oscillations in dysbiotic newborns underpin both the disrupted neutrophil maturation and macrophage dysfunction. We report that shared regulatory programs, anchored by circadian oscillations, inform the pathogenic remodeling of neutrophil and macrophage immune responses in dysbiotic newborn macaques. The intestinal microbiota undergoes diurnal compositional and functional oscillations (*133*), which, in turn, inform the homeostatic programming of host immune cells via clock genes, such as *BMAL1* and *NFIL3(83)*. Antibiotics disrupt these diurnal oscillations of the microbiota and lead to desynchronization of the circadian clock network both locally in the intestine and systemically (*133*). Circadian oscillations, anchored by BMAL1 and

NFIL3 in the sympathetic neurons, regulate the egress of neutrophils from the bone marrow into the periphery via CXCL12-dependent mechanism (*134*). Trafficking of neutrophils from blood to infected tissues is constrained by BMAL1-dependent regulation of CXCR4 and CCL2 expression (*135, 136*). A rhythmic release of CXCL5 from bronchiolar epithelial club cells promotes neutrophil recruitment in the lungs(*137*). Neutrophil aging and clearance of senescent neutrophils is regulated by circadian rhythms (*47*, *138*, *139*), and circadian clocks entrain the nature and amplitude of inflammatory responses in macrophages and T cells (*140*). Finally, NFIL3-driven circadian rhythms limit macrophage heterogeneity and amplify the pathogenic inflammatory responses in macrophages (*141*). These observations, coupled with our present data, suggest that disrupted circadian oscillations in dysbiotic newborns underpin both the disrupted neutrophil maturation and macrophage dysfunction.

The present study identifies dysfunctional macrophages as a 'central hub' of misdirected cell-cell communications. We report that rewired communication networks, anchored by dysfunctional macrophages, lead to global and cell-type specific maladaptations in dysbiotic newborn macaques. Our data demonstrated a stepwise engagement of tiered responses following respiratory infection. Macrophages and DCs sense respiratory pathogens and initiate immune responses, resulting in rapid recruitment of 'target cells,' such as neutrophils and T helper lymphocytes through the secretion of first-order cytokines, such as CXCR2/CXCL1 and CXCL8, IL1A, and IL1B/ILR2. Our study suggests that neutrophils and $CD4^+$ T cells transform the first-order cytokine signals into second-order cytokines that enhance the trafficking and extravasation (OSM-LIFR), immune co-activation (Complement C3-C3AR1), and effector function, such as phagocytosis (PTPRC-MRC1), to eliminate pathogens. At the same time, we report that reciprocal interactions limit macrophage activation (MIF-CD74/CXCR2 and CD83-PECAM1) and promote tissue-repair factors (CSF1-CSFR1, TGFBR3-TGFB1, SEMA4-NRP). Sequential engagement of these communication circuits ensures that the minimum necessary response to a microbe is engaged (**Supplemental Fig.6j**).

This stepwise, tiered response was disrupted in dysbiotic macaques due to dysfunctional macrophages. Immune-inhibitory interactions, such as CD274[PD-L1]-PDCD1, MIF-CD74/CD44/CXCR4, CD86-CD28, and PTPRC-CD22, which promote neutrophil and

lymphocyte dysfunction, dominated immune responses in dysbiotic newborns. Similarly, macrophage-anchored signaling pathways related to neutrophil migration, such as CXCL-CXCR2 and THBS1-CD47, neutrophil extravasation, such as ITGB2-ICAM1, and neutrophil activation, such as SELPLG-SELL, were disrupted in dysbiotic newborns (**Supplemental Fig.6j**). These changes in the communication circuits can potentially explain the shared hyperinflammatory signature in all immune cells and global loss of tissue-protective, homeostatic pathways. It may also explain the observed distinct patterns of immunoparalysis, such as dysregulated antigen presentation in the macrophages and impaired costimulatory function in T cells.

Finally, we show that fecal transfer systematically restores immune responses and protects the dysbiotic newborn against pneumonia. Our findings show that FT colonized the gut of dysbiotic newborns and shifted the composition of the recipient's microbiota toward *Gammaproteobacteria* and *Bifidobacterium bifidum,* taxa favoring immune response in humans. FT mitigated certain aspects of immune dysfunction seen in dysbiotic newborns. Remodeling of the neutrophil pool was partially corrected. Gene transcripts of genes related to leukocyte apoptosis, cellular stress, T cell activation, antigen processing, and presentation normalized, albeit partially, after FT. Gene transcripts related to macrophage maturation, tissue repair, and growth remain diminished. While broad dysregulation in signaling pathways related to inflammation, complement activation, and cell exhaustion was corrected in FT-recipients, miscommunication in pathways related to tissue repair and chemotaxis persisted.

Several scenarios may explain this partial restoration of specific aspects of immune responses in FT-recipient newborns. Distinct taxa drive the maturation of individual immune cells, so a lack of response may reflect the absence of favorable taxa in FT or failure of such taxa to engraft. A more logical explanation is that resolution of pneumonia requires a tiered response with the sequential engagement of innate immune cells and first-order cytokines, which activate other innate and adaptive immune cells via second-order cytokines. FT may not completely mitigate the disruption of such first- and second-order effectors, most likely due to persistent macrophage dysfunction, contributing to suboptimal benefit. Nevertheless, our study provides proof-of-concept evidence for the ability of FT to improve clinical outcomes in 'at-risk' dysbiotic newborns.

Our study has some limitations. The necessity of frequent clinical examination, sample collection, and invasive procedures precluded us from using dam-reared infants. Therefore, infants in our study received a diet consisting of formula, not breastmilk. As infants grow, feeding practices play an increasing role in determining the composition of the infant gut microbiota (*142-144*); however, delivery mode and perinatal antibiotic use have a stronger influence on the composition of the microbial community immediately after birth (*145*). Nevertheless, further studies are needed to delineate the relative contribution of infant diet to pulmonary immune maturation during infancy. Finally, mechanistic studies in murine models are necessary to test the hypotheses presented in this work.

In summary, our data suggest that divergence from the canonical innate and adaptive immune responses and tissue-repair programs, which are typically associated with resolution of pneumonia, leads to the clinical morbidity seen in dysbiotic newborns. We show that the immune response in dysbiotic newborns is marked by multifaceted dysfunction that is not uniformly hyperinflammatory. Although neutrophils and macrophages demonstrated augmented inflammatory signatures in dysbiotic newborns, we also observed distinct patterns of immunoparalysis, such as dysregulated antigen presentation by macrophages and T cells, impaired costimulatory function in T cells, and dysfunctional cytotoxic responses in NK cells, coupled with a global loss of tissue-protective, homeostatic pathways. The pathogenic remodeling of immune responses in dysbiotic newborns was also linked to disrupted circadian rhythms and anchored by miscommunication between dysfunctional macrophages and other effector cells.

Fecal microbiota transfer reversed some of these immune changes in dysbiotic newborn macaques and improved the clinical outcomes. Overall, our data suggest that gut microbiota reinforce the balance between regenerative pathways driving tissue homeostasis and inflammatory responses, limiting pathogens to promote clinical recovery and highlighting a potential role for fecal transfer as immune support in these 'at risk' infants.

MATERIALS AND METHODS:

Animal Husbandry: The Institutional Animal Care and Use Committee (IACUC) at Cincinnati Children's Hospital Medical Center and University of California at Davis approved all the animal studies (IACUC2016-19222), which were carried out in Association for the Assessment and Accreditation of Laboratory Animal Care (AAALAC)-accredited facilities at The California National Primate Research Center (CNPRC). Since there were no published studies in newborn primates, published data in newborn mice was used to estimate that four animals in each group would be sufficient to detect a 20% difference in morbidity with 80% power and an α of 0.05. Twelve vaginally delivered Indian origin rhesus macaque infants (*Macaca mulatta*) (**Supplemental Table 1**) were used in this study, which was conducted per NIH's *Guide for the Care and Use of Laboratory Animals.* Infant macaques were separated from their dams, raised in a nursery from the day of birth, and exposed to a normal light cycle (lights on for 12 h starting at 08:00). The infant macaques had a diet consisting of Enfamil Lipil + Iron for the duration of the study. The necessity of frequent clinical examination, sample collection, and invasive procedures precluded us from using dam-reared infants in our study. The infant macaques received either saline (n=4) or a cocktail of vancomycin, gentamicin, and ampicillin (n=4) from PN days 1-7. This antibiotic regimen targets both Gram-positive and Gram-negative intestinal bacteria and mimics antibiotic-exposure in human infants. At PN7, antibiotics were discontinued to allow 1 week of washout before subsequent infection on PN14.

Infectious studies: We grew *S. pneumoniae* serotype 19A (ATCC 700674) with gentle aeration (37°C, 200 rpm) in tryptic soy (TS) broth to log-phase growth. Neonatal macaques were inoculated with *S. pneumoniae* (10^6 CFU) via the intratracheal route on PN14. The newborn macaques were sedated with intramuscular Ketamine. Under direct visualization, aided by laryngoscope, *S. pneumoniae* (10^6 CFU in 1 ml of saline) was instilled into the trachea via an 8F feeding tube. After recovery, newborns were returned to the nursery. Vital signs, including heart rate, respiratory effort, blood pressure, urine output, oxygen saturation, and overall clinical condition of these newborn macaques were monitored every 6 hours. Chest radiographs were obtained daily. Sixty hours post-infection, the newborn macaques were euthanized.

Fecal transplant: Fecal transplants (FT) were performed in newborn macaques who had received the cocktail of vancomycin, gentamicin, and ampicillin from PN days 1-7. Pooled fecal contents from PN7 saline-treated newborn infants were homogenized in phosphate-buffered saline (PBS), and fibrous material was filtered out using a 70-µm-pore-size filter. The solution was centrifuged (100 x g), and the pellet was resuspended in PBS with 10% glycerol and frozen at -80°C for later use as donor microbiota. For transplantation, 25 g of fecal donor material was thawed for each FT-recipient animal, resuspended in 20 ml PBS, and gavaged into the duodenum via an endoscope after sedating the infant macaques on PN8. FT-recipient infants (n=4) were inoculated with *S. pneumoniae* (10^6 CFU) on PN14.

Microbiota analysis: Fecal samples were collected daily (PN1 to PN14) from saline treated (control) or antibiotic-treated (dysbiotic infants) infants. Fecal samples were collected daily (PN10 to PN14) in FT-recipient infants. Fecal samples were frozen (-80°C) immediately after collection. All samples were analyzed together to prevent batch effects. Frozen stool specimens were thawed, and DNA was extracted from them using Purelink Microbiome DNA purification kit (Invitrogen, USA) according to the manufacturer's instructions, including two-minutes use of a bead-beater (BioSpec, USA). The V4 region of the 16S gene was amplified with primers 515FB/806RB following protocols of the Illumina 16S amplicon protocols of the Earth Microbiome Project (http://press.igsb.anl.gov/earthmicrobiome/protocols-and-standards/16s/) and sequenced using an Illumina MiSeq. We merged ~21 million paired reads using fastq-join, to obtain ~12 million assembled 16S amplicon sequences.

After quality filtering, demultiplexing with split_libraries_fastq.py of QIIME v. 1.9.1, and further processing with vsearch v. 1.11.1(*146*), we identified ~90,000 operational taxonomic units (OTUs). Subsequent taxonomic assignment against the 16S reference sequence set of SILVA, v. 1.28(*147*), OTU sequence alignment, and generation of an unrooted phylogenetic tree, was performed in QIIME. A basic statistical diversity analysis was performed, using core_diversity_analysis.py of QIIME, including alpha-/beta-diversity and relative taxa abundances in sample groups. The determined relative taxa abundances were further analyzed with LEfSe (Linear discriminant analysis effect size)(*148*), to identify differential biomarkers in sample groups. Alpha-diversity analysis

was performed on samples after rarefaction to 10000 sequences/sample (minimum sampling depth). Rarefaction curves were generated for the phylogenetic distance between two groups. Phylogenetic distance was calculated at a rarefaction depth of 10000 sequences per sample.

The Analysis of Composition of Microbiomes (ANCOM) test(*149*) was used for differential taxonomical analysis with abundance datasets of all taxonomic levels between groups using the FDR cutoff of 0.05. The ANCOM test provides a W-statistic score for each taxon and logical indicators demonstrating whether a taxon is differentially abundant. The ANCOM test also provides a CLR (conditional likelihood ratio test) F-statistic score, which accounts for the effect-size difference of each taxon between two groups. Higher F- and W-scores indicate a higher probability for the taxa to be truly different across groups. Volcano plots were generated with W-statistic on the y-axis, and the F-score (CLR mean difference) on the x-axis using an R package ggplot2(*150*). Heatmaps were created using "pheatmap" for R (RStudio version 1.1.463, based on R version 3.5.1).

Tissue processing: Whole blood (20 ml), lungs (left lobes), and bronchial washings were harvested. Lung lobes and a portion of whole blood (10 ml) were shipped overnight in preservative (Histidine-tryptophan-ketoglutarate [HTK] solution for lungs and EDTA tubes for whole blood) and processing the following day. Remaining whole blood was centrifuged (2,000g, 10 min, 4˚C) without brake to separate the cells and plasma within 6 hours of collection. Cells were resuspended in RPMI with 10% FCS, slow frozen using a Mr. Frosty device, and stored at -80˚C till further analysis. Plasma separated from the cells was frozen at -80˚C till further analysis. Alveolar wash was centrifuged (2,000 x g, 10 min, 4˚C) and cells were spun onto glass slides using a Cytospin 4 Cytocentrifuge (Thermo Scientific), dried for 10 min, fixed in methanol, and stained with the Hema 3 manual staining system (Fisher Diagnostics) to identify different immune cells. Supernatant was frozen at -80˚C till further analysis. Lung lobes were shipped overnight in preservative (HTK solution) and processed the following day. Lung pieces were diced into approximately 1 cm cubes and incubated (37 °C, 30 min.) with the cut tissues shaking (200 rpm) in digestion buffer (RPMI 1640 with 10% FCS, 15 mM HEPES, 1% penicillin/streptomycin [wt/vol] and 300 U/mL collagenase VIII) and pressed through

a 100-μm nylon strainer to obtain a single-cell suspension. The resulting single-cell suspension from the lung was then enriched via magnetic cell separation for $CD326^{-}CD31^{-}CD45^{+}$ cells and slow frozen until further analysis.

Plasma proteins and bronchial lavage cytokine profiling: Frozen plasma samples or frozen alveolar washes were thawed and analyzed together to prevent batch effects. A custom, premixed, bead-based multiplex kit for Non-Human Primate Cytokines (Cat # EPX370-40045-901, ThermoFisher Scientific) was used according to manufacturer instructions. This kit included premixed beads for ~ 30 cytokines: G-CSG, GM-CSF, IFNγ, IP-10 (CXCL10), IL1β, IL1RA, IL2, IL4, IL5, IL6, IL8 (CXCL8), IL10, IL12/23 (p40), IL15, IL17, CCL2 (MCP-1), CCL3 (MIP-1α), CCL4 (MIP-1β), CCL5 (RANTES), CXCL9 (MIG), I-TAC (CXCL11), TNFα, EGF, VEGF-A, HGF, PDGF-AA, PDGF-BB, CD40L and CD274 (PD-L1). Standard curves for each cytokine were prepared by serial dilution and run-in triplicate (1–10,000 pg/mL for all cytokines). The manufacturer reports "no or negligible" cross-reactivity between any of the analytes of the assay panel. A Luminex 100 system equipped with xPONENT v. 3.1 software was used to determine the median fluorescent index and calculate the concentration for each cytokine**.** ATP concentrations in alveolar washes were measured using an ATP Determination Kit (BioAssay Systems) and a luminometer as described previously(*151*). The values were normalized and heatmaps were created using "pheatmap" for R.

CyTOF: Frozen whole blood leukocytes or $CD326^{-}CD31^{-}CD45^{+}$ pulmonary cells were thawed and plated at 1×10^{6} cells per well in a 96-well U-bottom plate. All samples were analyzed together to prevent batch effects. Cells were incubated (4 °C, 20 min) in Live/Dead Fixable Aqua (ThermoFisher). Following a wash, cells were incubated (RT, 10 min) with Rhesus Fc Receptor Binding Polyclonal Antibody (Biolegend). Desired staining antibodies were added directly to this mixture at indicated dilutions (**Supplemental Table 27**) and cells were further incubated (RT, 30 min). For intracellular cytokine staining, cells were incubated (RT, 1 hr) with 1× Cell Stimulation Cocktail plus protein transport 442 inhibitor (eBioscience, Cat # 00-4970-93). Following stimulation, cells were washed and resuspended in 100 µl 4% PFA (4 °C, 30 min). To quantify intracellular cytokines, these samples were permeabilized with 1× permeabilization buffer from the FOXP3/Transcription Factor Staining Buffer Set (eBioscience) (4 °C, 10 min). All

subsequent staining cocktails were made in this buffer. Finally, intracellular-staining antibodies were added directly to this mixture and cells were further incubated (RT, 30 min). Following this incubation, cells were washed and prepared for analysis by CyTOF (Fluidigm). Data were analyzed using FlowJo software version 10.6 software (Tree S-tar). The specific sets of markers used to identify each subset of cells are summarized in **Supplemental Fig. 1c**.

After manually excluding EQ beads, dead cells, doublets, and debris, further clustering analysis was performed using the FlowSOM plugin in FlowJo 10.4.1 on arcsinh-transformed data using a grid size of 10x10. Eleven main cell lineages in the data were identified (Naïve $CD4^+$ and $CD8^+$ T cells, cytotoxic $CD8^+$ T cells, B cells, $CD56^{bright}$NK cells, $CD56^{dim}$NK cells, $CD14^+$ and $CD16^+$ monocytes, neutrophils and dendritic cells) and shown as an overlay on the tSNE projection (**Supplemental Fig. 1a**) and as Minimum Spanning Tree projection (**Supplemental Fig. 1b**). To precisely describe the phenotypic landscape of the neutrophils and $CD4^+$ T cells, the dataset was further partitioned/clustered using the FlowSOM algorithm, resulting in several clusters. Overall similarity of neutrophils and $CD4^+$ T cells in each sample compared to all other samples was evaluated by agglomerative hierarchical clustering using Euclidean distance metric and Ward's linkage criterion within the FlowSOM plugin in FlowJo 10.4.1.

Single-cell RNA-sequencing and data analysis: Frozen $CD326^-CD31^-CD45^+$ cells from digested lungs were thawed and resuspended in 50 μL at a concentration of 1000 cells/ μL. After excluding dead cells, ~20,000 cells (~3-4000 cells per animal, barcoded to identify individual animals) were then loaded into one channel of the Chromium system using the v3 single cell reagent kit (10X Genomics, Pleasanton, CA) at the Cincinnati Children's Hospital Medical Center DNA Sequencing and Genotyping Core. Following capture and lysis, cDNA was synthesized and amplified as per the manufacturer's protocol (10X Genomics). The amplified cDNA was used to construct Illumina sequencing libraries that were each sequenced using an Illumina HiSeq 4000.

Alignment and Quality Control: Raw sequencing data (submitted to Gene Expression Omnibus, Accession number GSE176408) were aligned to the Rhesus macaque reference Mmul_10 with Cell Ranger 1.3 (10X Genomics), generating expression count matrix files

(**see Supplemental Table 28 for dataset metrics**). Cells that had fewer than 750 UMIs or greater than 15,000 UMIs, as well as cells that contained greater than 20% of reads from mitochondrial genes or rRNA genes (RNA18S5 or RNA28S5) or hemoglobin genes, were considered low quality and removed from further analysis. Putative multiplets were removed with DoubletFinder (version 2.0). Genes that were expressed in fewer than 10 cells were removed from the final count matrix.

Data analysis: The Seurat package (version 3.1.0, https://satijalab.org/seurat/) was used to identify common cell types across different experimental conditions, differential expression analysis, and most visualizations. Percentages of mitochondrial, ribosomal genes, and hemoglobin genes were regressed during data scaling to remove unwanted variation due to cell quality using the SCTransform () function in Seurat. PCA was performed using the 3,000 most highly variable genes, and the first 20 principal components (PCs) were used to perform UMAP to embed the dataset into two dimensions. Next, the first 20 PCs were used to construct a shared nearest neighbor graph (SNN; FindNeighbors ()) and this SNN used to cluster the dataset (FindClusters ()). Manual annotation of cellular identity was performed by finding differentially expressed genes for each cluster using Seurat's implementation of the Wilcoxon rank-sum test (FindMarkers()) and comparing those markers to known cell type-specific genes from published studies (*37*)(*38*). Global differential gene expression profiles between all cell types were identified and organized with the software cellHarmony (*152*), using these Seurat clusters (fold change > 1.2, empirical Bayes t-test p-value <0.05, FDR corrected)

Automated annotation of T cell subsets: This annotation was performed using web application (https://azimuth.hubmapconsortium.org) (*153*). Anchors between the reference (multimodal reference dataset of > 100,000 PBMC) and our dataset were identified using a precomputed, supervised PCA of the reference dataset that maximally captures the structure of the weighted n neighbor (WNN) graph. Cell type labels from the reference dataset were transferred to each cell of the query data set through previously identified anchors.

For pathway and gene ontology analysis: Differentially expressed genes between control and dysbiotic infants within neutrophil, AM, and IM populations with a fold change of ≥

1.2 and t-test p-value of ≤ 0.05 (FDR corrected) were used for functional enrichment analysis of biological processes and pathways using the ToppFun web portal (*154*) or GO-Elite (*155*). Overrepresented pathways in each subcluster were visualized with ggplot2.

Gene module scoring analysis: Seurat function AddModuleScore() (*38*) was used to score single cells by expression of a list of genes of interest. This function calculates a module score by comparing the expression level of an individual query gene to other randomly selected control genes expressed at similar levels to the query genes, allowing a robust method for scoring modules containing both lowly and highly expressed genes and scoring cells with different sequencing depths. Gene lists used to define each module for neutrophils or AMs are listed in **Supplemental Table 12** and **Supplemental table 17**, respectively. For bulk transcriptomic datasets, including neutrophil degranulation[49], LPS-stimulated PD-L1^{+} neutrophils (*156*) or neutrophils from ARDS-complicated sepsis (*157*) or alveolar macrophages from ARDS (*46, 158*), the top 97th percentile of differentially expressed genes relative to control samples/patients were used for scoring.

Inflammatory cytokine score-related subtypes analysis: To define inflammatory cytokine score, we downloaded a gene set termed 'HALLMARK_INFLAMMATORY_RESPONSE' from MSigDB (*159*) and collected cytokine genes. Seurat function AddModuleScore() (*38*) was used to score single cells by expression of inflammatory cytokine genes. To select the most promising hyperinflammatory cell types, we performed a Mann-Whitney rank test (single-tail) for each subtype's score versus all the other subtypes' score. Three subtypes (AMs, IMs, and Neutrophils) were defined as hyperinflammatory cell types with significantly statistical parameters ($p < 0.001$) in both cytokine inflammatory scores.

Assessment of different trajectory states of gene expression: Within neutrophils or AMs, single-cell trajectory analysis was performed using Monocle3 (*49*) (version 0.2.3.0). Spatial autocorrelation analysis as implemented in Monocle3 was used to determine genes that most strongly vary along the pseudotime trajectory. The Monocle algorithm is capable of ordering cells based on their transcriptomic profile in an unsupervised manner and thus arrange cells along a directional path. The order of the cells along this path

represents different transcriptomic states within a biological process even if cells are obtained at only one time point during an experiment.

Identification of transcription factors: We predicted transcription factors regulating neutrophil or AM heterogeneity using *SCENIC* (single-cell regulatory network inference and clustering) (*160*). Default parameters were used for the *SCENIC* workflow in R and the normalized single-cell gene expression matrix for neutrophils or AMs from Seurat was used as input. Co-expression analysis was performed with *GENIE3 (161)*. For visualization, we calculated the average regulon activity (AUC) scores for each neutrophil cluster and selected the top regulons to plot as a heatmap using R package "pheatmap".

Annotation of macrophage development and activation states: We used *MacSpectrum(77)* for comprehensive analysis of heterogeneous macrophage subpopulations, including the identification of condition-specific signature genes. Default parameters were used for the *Macspectrum* workflow in R and the normalized single-cell gene expression matrix for AM or IM from Seurat was used as input to derive a macrophage polarization index (MPI) and activation-induced macrophage differentiation index (AMDI) for each cell. Higher MPI suggests more M1-like (more inflammatory) states and lower MPI suggests more M2-like (less inflammatory) states. AMDI value depicts relative maturity of macrophages with a higher AMDI value indicating a more mature macrophage.

Investigation of cell-cell communication networks: We used CellChat workflow with default parameters in R (*98*). A normalized single-cell gene expression matrix from Seurat was used as input. We limited the cell-cell communication inferences to the following major cell types: Neutrophils, AMs, IMs, B cells, NK cells, cDC and pDC. Circle plots depicting strength of cell-cell communication and dot-plots indicating communication probabilities were generated using CellChat as described before (*98*).

Mortality prediction using senescent neutrophil DEGs: To test whether the gene signature of senescent neutrophils could be used to predict mortality, we first developed a five-gene signature of the senescent neutrophils by identifying the most differentially

enriched genes in cluster 2 neutrophils in our transcriptomic dataset relative to all other cells. Next, we downloaded normalized transcript counts from a publicly available whole blood bulk transcriptomic dataset (GSE696686) (*59*). We then scored each sample in this dataset by the expression of the five genes enriched in our senescent neutrophil cluster (*HIF1A*, *CXCR4*, *CD274*, *LTF*, and *S100A8*). Finally, we used these gene signature scores as a predictor variable and disease severity metadata reported by Wynn et al.(*59*) as the response variable to construct an ROC curve to quantify and visualize the sensitivity and specificity of the prediction.

Statistical Tests: All data met the assumptions of the statistical tests used. Statistical tests used for microbiome or single-cell analyses are described in relevant sections. For comparing the differences between groups, we used either unpaired two-tailed Student's *t*-test or ANOVA or Wilcoxon signed-rank test. We used Pearson correlation coefficient to measure correlation between different variables. We used the Kaplan-Meier log-rank test to compare morbidity between groups (All in GraphPad Prism 8.0). *P*-values are indicated as follows: * $p \leq 0.05$ or ** $p \leq 0.01$. Due to the limited number of samples in some groups, we also report trends.

REFERENCES:

1. D. J. Dowling, O. Levy, Ontogeny of early life immunity. *Trends Immunol* **35**, 299-310 (2014).
2. D. M. MacGillivray, T. R. Kollmann, The role of environmental factors in modulating immune responses in early life. *Front Immunol* **5**, 434 (2014).
3. H. L. Cash, C. V. Whitham, C. L. Behrendt, L. V. Hooper, Symbiotic bacteria direct expression of an intestinal bactericidal lectin. *Science* **313**, 1126-1130 (2006).
4. E. Elinav, T. Strowig, J. Henao-Mejia, R. A. Flavell, Regulation of the antimicrobial response by NLR proteins. *Immunity* **34**, 665-679 (2011).
5. H. S. Deshmukh *et al.*, The microbiota regulates neutrophil homeostasis and host resistance to Escherichia coli K1 sepsis in neonatal mice. *Nat Med* **20**, 524-530 (2014).
6. M. G. Rooks, W. S. Garrett, Gut microbiota, metabolites and host immunity. *Nat Rev Immunol* **16**, 341-352 (2016).
7. T. P. Wypych, L. C. Wickramasinghe, B. J. Marsland, The influence of the microbiome on respiratory health. *Nat Immunol* **20**, 1279-1290 (2019).
8. J. Y. Ting *et al.*, Association Between Antibiotic Use and Neonatal Mortality and Morbidities in Very Low-Birth-Weight Infants Without Culture-Proven Sepsis or Necrotizing Enterocolitis. *JAMA Pediatr* **170**, 1181-1187 (2016).
9. R. H. Clark, B. T. Bloom, A. R. Spitzer, D. R. Gerstmann, Reported medication use in the neonatal intensive care unit: data from a large national data set. *Pediatrics* **117**, 1979-1987 (2006).
10. R. Spaetgens *et al.*, Perinatal antibiotic usage and changes in colonization and resistance rates of group B streptococcus and other pathogens. *Obstet Gynecol* **100**, 525-533 (2002).
11. F. Y. Lin *et al.*, Assessment of intrapartum antibiotic prophylaxis for the prevention of early-onset group B Streptococcal disease. *Pediatr Infect Dis J* **30**, 759-763 (2011).
12. M. Knight *et al.*, Prophylactic antibiotics in the prevention of infection after operative vaginal delivery (ANODE): a multicentre randomised controlled trial. *Lancet* **393**, 2395-2403 (2019).
13. V. S. Kuppala, J. Meinzen-Derr, A. L. Morrow, K. R. Schibler, Prolonged initial empirical antibiotic treatment is associated with adverse outcomes in premature infants. *The Journal of pediatrics* **159**, 720-725 (2011).
14. R. H. Clark, B. T. Bloom, A. R. Spitzer, D. R. Gerstmann, Empiric use of ampicillin and cefotaxime, compared with ampicillin and gentamicin, for neonates at risk for sepsis is associated with an increased risk of neonatal death. *Pediatrics* **117**, 67-74 (2006).
15. C. M. Cotten *et al.*, Prolonged duration of initial empirical antibiotic treatment is associated with increased rates of necrotizing enterocolitis and death for extremely low birth weight infants. *Pediatrics* **123**, 58-66 (2009).
16. V. Mai *et al.*, Distortions in development of intestinal microbiota associated with late onset sepsis in preterm infants. *PloS one* **8**, e52876 (2013).
17. S. Arboleya *et al.*, Intestinal microbiota development in preterm neonates and effect of perinatal antibiotics. *The Journal of pediatrics* **166**, 538-544 (2015).
18. L. A. Miller, C. M. Royer, K. E. Pinkerton, E. S. Schelegle, Nonhuman Primate Models of Respiratory Disease: Past, Present, and Future. *ILAR J* **58**, 269-280 (2017).

19. L. Tao, T. A. Reese, Making Mouse Models That Reflect Human Immune Responses. *Trends Immunol* **38**, 181-193 (2017).
20. M. T. Philipp *et al.*, Experimental infection of rhesus macaques with Streptococcus pneumoniae: a possible model for vaccine assessment. *J Med Primatol* **35**, 113-122 (2006).
21. C. Palmer, E. M. Bik, D. B. DiGiulio, D. A. Relman, P. O. Brown, Development of the human infant intestinal microbiota. *PLoS biology* **5**, e177 (2007).
22. J. A. Gilbert *et al.*, Current understanding of the human microbiome. *Nat Med* **24**, 392-400 (2018).
23. E. Weirich *et al.*, Neutrophil CD11b expression as a diagnostic marker for early-onset neonatal infection. *The Journal of pediatrics* **132**, 445-451 (1998).
24. H. T. Jin *et al.*, Cooperation of Tim-3 and PD-1 in CD8 T-cell exhaustion during chronic viral infection. *Proceedings of the National Academy of Sciences of the United States of America* **107**, 14733-14738 (2010).
25. A. H. Sharpe, K. E. Pauken, The diverse functions of the PD1 inhibitory pathway. *Nat Rev Immunol* **18**, 153-167 (2018).
26. A. Johannisson, R. Festin, Phenotype transition of CD4+ T cells from CD45RA to CD45R0 is accompanied by cell activation and proliferation. *Cytometry* **19**, 343-352 (1995).
27. E. J. Wherry, M. Kurachi, Molecular and cellular insights into T cell exhaustion. *Nat Rev Immunol* **15**, 486-499 (2015).
28. H. Kared, S. Martelli, T. P. Ng, S. L. Pender, A. Larbi, CD57 in human natural killer cells and T-lymphocytes. *Cancer Immunol Immunother* **65**, 441-452 (2016).
29. F. Morandi *et al.*, CD38, a Receptor with Multifunctional Activities: From Modulatory Functions on Regulatory Cell Subsets and Extracellular Vesicles, to a Target for Therapeutic Strategies. *Cells* **8**, (2019).
30. P. Khandelwal *et al.*, CD38(bright)CD8(+) T Cells Associated with the Development of Acute GVHD Are Activated, Proliferating, and Cytotoxic Trafficking Cells. *Biol Blood Marrow Transplant* **26**, 1-6 (2020).
31. M. Ostapchuk, D. M. Roberts, R. Haddy, Community-acquired pneumonia in infants and children. *Am Fam Physician* **70**, 899-908 (2004).
32. H. Duncan, J. Hutchison, C. S. Parshuram, The Pediatric Early Warning System score: a severity of illness score to predict urgent medical need in hospitalized children. *J Crit Care* **21**, 271-278 (2006).
33. J. Rello, V. Ausina, M. Ricart, J. Castella, G. Prats, Impact of previous antimicrobial therapy on the etiology and outcome of ventilator-associated pneumonia. *Chest* **104**, 1230-1235 (1993).
34. P. L. Ho *et al.*, Risk factors for acquisition of levofloxacin-resistant Streptococcus pneumoniae: a case-control study. *Clin Infect Dis* **32**, 701-707 (2001).
35. S. P. Kuster *et al.*, Previous antibiotic exposure and antimicrobial resistance in invasive pneumococcal disease: results from prospective surveillance. *Clin Infect Dis* **59**, 944-952 (2014).
36. A. Boutten *et al.*, Compartmentalized IL-8 and elastase release within the human lung in unilateral pneumonia. *Am J Respir Crit Care Med* **153**, 336-342 (1996).
37. K. J. Travaglini *et al.*, A molecular cell atlas of the human lung from single-cell RNA sequencing. *Nature* **587**, 619-625 (2020).
38. T. Stuart *et al.*, Comprehensive Integration of Single-Cell Data. *Cell* **177**, 1888-1902 e1821 (2019).

39. M. Brandes, F. Klauschen, S. Kuchen, R. N. Germain, A systems analysis identifies a feedforward inflammatory circuit leading to lethal influenza infection. *Cell* **154**, 197-212 (2013).
40. H. I. Nakaya *et al.*, Systems Analysis of Immunity to Influenza Vaccination across Multiple Years and in Diverse Populations Reveals Shared Molecular Signatures. *Immunity* **43**, 1186-1198 (2015).
41. A. J. Wilk *et al.*, A single-cell atlas of the peripheral immune response in patients with severe COVID-19. *Nat Med* **26**, 1070-1076 (2020).
42. R. A. Grant *et al.*, Circuits between infected macrophages and T cells in SARS-CoV-2 pneumonia. *Nature* **590**, 635-641 (2021).
43. A. F. Rendeiro *et al.*, The spatial landscape of lung pathology during COVID-19 progression. *Nature*, (2021).
44. T. Wang *et al.*, Single-cell RNA sequencing reveals the sustained immune cell dysfunction in the pathogenesis of sepsis secondary to bacterial pneumonia. *Genomics* **113**, 1219-1233 (2021).
45. L. G. Ng, R. Ostuni, A. Hidalgo, Heterogeneity of neutrophils. *Nat Rev Immunol* **19**, 255-265 (2019).
46. M. Reyes *et al.*, An immune-cell signature of bacterial sepsis. *Nat Med* **26**, 333-340 (2020).
47. D. Zhang *et al.*, Neutrophil ageing is regulated by the microbiome. *Nature* **525**, 528-532 (2015).
48. L. A. O'Neill, R. J. Kishton, J. Rathmell, A guide to immunometabolism for immunologists. *Nat Rev Immunol* **16**, 553-565 (2016).
49. J. Cao *et al.*, The single-cell transcriptional landscape of mammalian organogenesis. *Nature* **566**, 496-502 (2019).
50. X. Qiu *et al.*, Single-cell mRNA quantification and differential analysis with Census. *Nat Methods* **14**, 309-315 (2017).
51. X. Qiu *et al.*, Reversed graph embedding resolves complex single-cell trajectories. *Nat Methods* **14**, 979-982 (2017).
52. C. Trapnell *et al.*, The dynamics and regulators of cell fate decisions are revealed by pseudotemporal ordering of single cells. *Nat Biotechnol* **32**, 381-386 (2014).
53. M. A. Khan, N. Palaniyar, Transcriptional firing helps to drive NETosis. *Sci Rep* **7**, 41749 (2017).
54. P. R. Nagareddy *et al.*, NETosis Is Required for S100A8/A9-Induced Granulopoiesis After Myocardial Infarction. *Arterioscler Thromb Vasc Biol* **40**, 2805-2807 (2020).
55. A. H. Sharpe, E. J. Wherry, R. Ahmed, G. J. Freeman, The function of programmed cell death 1 and its ligands in regulating autoimmunity and infection. *Nat Immunol* **8**, 239-245 (2007).
56. T. Narasaraju *et al.*, Excessive neutrophils and neutrophil extracellular traps contribute to acute lung injury of influenza pneumonitis. *Am J Pathol* **179**, 199-210 (2011).
57. Y. Li *et al.*, B7H3 ameliorates LPS-induced acute lung injury via attenuation of neutrophil migration and infiltration. *Sci Rep* **6**, 31284 (2016).
58. J. Bordon *et al.*, Understanding the roles of cytokines and neutrophil activity and neutrophil apoptosis in the protective versus deleterious inflammatory response in pneumonia. *Int J Infect Dis* **17**, e76-83 (2013).
59. J. L. Wynn *et al.*, Postnatal Age Is a Critical Determinant of the Neonatal Host Response to Sepsis. *Mol Med* **21**, 496-504 (2015).

60. J. Turner, M. Crossley, Basic Kruppel-like factor functions within a network of interacting haematopoietic transcription factors. *Int J Biochem Cell Biol* **31**, 1169-1174 (1999).
61. N. Matsumoto *et al.*, Developmental regulation of yolk sac hematopoiesis by Kruppel-like factor 6. *Blood* **107**, 1357-1365 (2006).
62. A. Cloutier *et al.*, Inflammatory cytokine production by human neutrophils involves C/EBP transcription factors. *J Immunol* **182**, 563-571 (2009).
63. Z. Cao, X. Sun, B. Icli, A. K. Wara, M. W. Feinberg, Role of Kruppel-like factors in leukocyte development, function, and disease. *Blood* **116**, 4404-4414 (2010).
64. M. Humbert *et al.*, Deregulated expression of Kruppel-like factors in acute myeloid leukemia. *Leuk Res* **35**, 909-913 (2011).
65. S. M. Lawrence, R. Corriden, V. Nizet, The Ontogeny of a Neutrophil: Mechanisms of Granulopoiesis and Homeostasis. *Microbiol Mol Biol Rev* **82**, (2018).
66. A. Oeckinghaus, M. S. Hayden, S. Ghosh, Crosstalk in NF-kappaB signaling pathways. *Nat Immunol* **12**, 695-708 (2011).
67. W. Liao, J. X. Lin, W. J. Leonard, IL-2 family cytokines: new insights into the complex roles of IL-2 as a broad regulator of T helper cell differentiation. *Curr Opin Immunol* **23**, 598-604 (2011).
68. T. Sun *et al.*, Intestinal Batf3-dependent dendritic cells are required for optimal antiviral T-cell responses in adult and neonatal mice. *Mucosal Immunol* **10**, 775-788 (2017).
69. D. M. Schwartz *et al.*, Retinoic Acid Receptor Alpha Represses a Th9 Transcriptional and Epigenomic Program to Reduce Allergic Pathology. *Immunity* **50**, 106-120 e110 (2019).
70. S. Kamizono *et al.*, Nfil3/E4bp4 is required for the development and maturation of NK cells in vivo. *J Exp Med* **206**, 2977-2986 (2009).
71. F. Sommer, I. Nookaew, N. Sommer, P. Fogelstrand, F. Backhed, Site-specific programming of the host epithelial transcriptome by the gut microbiota. *Genome Biol* **16**, 62 (2015).
72. Y. Wang *et al.*, The intestinal microbiota regulates body composition through NFIL3 and the circadian clock. *Science* **357**, 912-916 (2017).
73. R. Orozco-Solis, L. Aguilar-Arnal, Circadian Regulation of Immunity Through Epigenetic Mechanisms. *Front Cell Infect Microbiol* **10**, 96 (2020).
74. J. Day, A. Friedman, L. S. Schlesinger, Modeling the immune rheostat of macrophages in the lung in response to infection. *Proceedings of the National Academy of Sciences of the United States of America* **106**, 11246-11251 (2009).
75. T. Hussell, T. J. Bell, Alveolar macrophages: plasticity in a tissue-specific context. *Nat Rev Immunol* **14**, 81-93 (2014).
76. M. Guilliams, F. R. Svedberg, Does tissue imprinting restrict macrophage plasticity? *Nat Immunol* **22**, 118-127 (2021).
77. C. Li *et al.*, Single cell transcriptomics based-MacSpectrum reveals novel macrophage activation signatures in diseases. *JCI Insight* **5**, (2019).
78. B. Allard, A. Panariti, J. G. Martin, Alveolar Macrophages in the Resolution of Inflammation, Tissue Repair, and Tolerance to Infection. *Front Immunol* **9**, 1777 (2018).
79. S. Grazioli *et al.*, Mitochondrial alarmins are tissue mediators of ventilator-induced lung injury and ARDS. *PloS one* **14**, e0225468 (2019).

80. D. Langlais, L. B. Barreiro, P. Gros, The macrophage IRF8/IRF1 regulome is required for protection against infections and is associated with chronic inflammation. *J Exp Med* **213**, 585-603 (2016).
81. V. M. Link *et al.*, Analysis of Genetically Diverse Macrophages Reveals Local and Domain-wide Mechanisms that Control Transcription Factor Binding and Function. *Cell* **173**, 1796-1809 e1717 (2018).
82. S. E. Corcoran, L. A. O'Neill, HIF1alpha and metabolic reprogramming in inflammation. *J Clin Invest* **126**, 3699-3707 (2016).
83. C. A. Thaiss *et al.*, Microbiota Diurnal Rhythmicity Programs Host Transcriptome Oscillations. *Cell* **167**, 1495-1510 e1412 (2016).
84. D. You *et al.*, Inchoate CD8+ T cell responses in neonatal mice permit influenza-induced persistent pulmonary dysfunction. *J Immunol* **181**, 3486-3494 (2008).
85. I. Thevarajan *et al.*, Breadth of concomitant immune responses prior to patient recovery: a case report of non-severe COVID-19. *Nat Med* **26**, 453-455 (2020).
86. B. Diao *et al.*, Reduction and Functional Exhaustion of T Cells in Patients With Coronavirus Disease 2019 (COVID-19). *Front Immunol* **11**, 827 (2020).
87. D. Mathew *et al.*, Deep immune profiling of COVID-19 patients reveals distinct immunotypes with therapeutic implications. *Science* **369**, (2020).
88. T. Sekine *et al.*, Robust T Cell Immunity in Convalescent Individuals with Asymptomatic or Mild COVID-19. *Cell* **183**, 158-168 e114 (2020).
89. R. J. Salmond, mTOR Regulation of Glycolytic Metabolism in T Cells. *Front Cell Dev Biol* **6**, 122 (2018).
90. J. Jung, H. Zeng, T. Horng, Metabolism as a guiding force for immunity. *Nat Cell Biol* **21**, 85-93 (2019).
91. Z. Chen, E. John Wherry, T cell responses in patients with COVID-19. *Nat Rev Immunol* **20**, 529-536 (2020).
92. S. De Biasi *et al.*, Marked T cell activation, senescence, exhaustion and skewing towards TH17 in patients with COVID-19 pneumonia. *Nat Commun* **11**, 3434 (2020).
93. J. Y. Zhang *et al.*, Single-cell landscape of immunological responses in patients with COVID-19. *Nat Immunol* **21**, 1107-1118 (2020).
94. S. N. Waggoner, M. Cornberg, L. K. Selin, R. M. Welsh, Natural killer cells act as rheostats modulating antiviral T cells. *Nature* **481**, 394-398 (2011).
95. S. Malarkannan, NKG7 makes a better killer. *Nat Immunol* **21**, 1139-1140 (2020).
96. S. L. Smith *et al.*, Diversity of peripheral blood human NK cells identified by single-cell RNA sequencing. *Blood Adv* **4**, 1388-1406 (2020).
97. R. J. Miragaia *et al.*, Single-Cell Transcriptomics of Regulatory T Cells Reveals Trajectories of Tissue Adaptation. *Immunity* **50**, 493-504 e497 (2019).
98. S. Jin *et al.*, Inference and analysis of cell-cell communication using CellChat. *Nat Commun* **12**, 1088 (2021).
99. W. A. Muller, S. A. Weigl, X. Deng, D. M. Phillips, PECAM-1 is required for transendothelial migration of leukocytes. *J Exp Med* **178**, 449-460 (1993).
100. P. J. Mansfield, S. J. Suchard, Thrombospondin promotes chemotaxis and haptotaxis of human peripheral blood monocytes. *J Immunol* **153**, 4219-4229 (1994).
101. S. Alampour-Rajabi *et al.*, MIF interacts with CXCR7 to promote receptor internalization, ERK1/2 and ZAP-70 signaling, and lymphocyte chemotaxis. *FASEB J* **29**, 4497-4511 (2015).

102. Y. Takai, J. Miyoshi, W. Ikeda, H. Ogita, Nectins and nectin-like molecules: roles in contact inhibition of cell movement and proliferation. *Nat Rev Mol Cell Biol* **9**, 603-615 (2008).
103. S. Chigurupati *et al.*, Involvement of notch signaling in wound healing. *PloS one* **2**, e1167 (2007).
104. J. Xia *et al.*, Semaphorin-Plexin Signaling Controls Mitotic Spindle Orientation during Epithelial Morphogenesis and Repair. *Dev Cell* **33**, 299-313 (2015).
105. A. Nolan *et al.*, Differential role for CD80 and CD86 in the regulation of the innate immune response in murine polymicrobial sepsis. *PloS one* **4**, e6600 (2009).
106. M. Bokarewa, I. Nagaev, L. Dahlberg, U. Smith, A. Tarkowski, Resistin, an adipokine with potent proinflammatory properties. *J Immunol* **174**, 5789-5795 (2005).
107. M. Mourtada-Maarabouni, V. L. Hedge, L. Kirkham, F. Farzaneh, G. T. Williams, Growth arrest in human T-cells is controlled by the non-coding RNA growth-arrest-specific transcript 5 (GAS5). *J Cell Sci* **121**, 939-946 (2008).
108. Y. Latchman *et al.*, PD-L2 is a second ligand for PD-1 and inhibits T cell activation. *Nat Immunol* **2**, 261-268 (2001).
109. A. C. Patera *et al.*, Frontline Science: Defects in immune function in patients with sepsis are associated with PD-1 or PD-L1 expression and can be restored by antibodies targeting PD-1 or PD-L1. *J Leukoc Biol* **100**, 1239-1254 (2016).
110. V. Gopalakrishnan *et al.*, Gut microbiome modulates response to anti-PD-1 immunotherapy in melanoma patients. *Science* **359**, 97-103 (2018).
111. Y. Zhang *et al.*, PD-L1 blockade improves survival in experimental sepsis by inhibiting lymphocyte apoptosis and reversing monocyte dysfunction. *Crit Care* **14**, R220 (2010).
112. V. Matson *et al.*, The commensal microbiome is associated with anti-PD-1 efficacy in metastatic melanoma patients. *Science* **359**, 104-108 (2018).
113. B. Routy *et al.*, Gut microbiome influences efficacy of PD-1-based immunotherapy against epithelial tumors. *Science* **359**, 91-97 (2018).
114. D. Zheng, T. Liwinski, E. Elinav, Interaction between microbiota and immunity in health and disease. *Cell Res* **30**, 492-506 (2020).
115. A. T. Vieira *et al.*, Oral treatment with Bifidobacterium longum 51A reduced inflammation in a murine experimental model of gout. *Benef Microbes* **6**, 799-806 (2015).
116. A. T. Vieira *et al.*, Control of Klebsiella pneumoniae pulmonary infection and immunomodulation by oral treatment with the commensal probiotic Bifidobacterium longum 5(1A). *Microbes Infect* **18**, 180-189 (2016).
117. J. L. Gehrig *et al.*, Effects of microbiota-directed foods in gnotobiotic animals and undernourished children. *Science* **365**, (2019).
118. S. Subramanian *et al.*, Persistent gut microbiota immaturity in malnourished Bangladeshi children. *Nature* **510**, 417-421 (2014).
119. P. Brodin, D. Duffy, L. Quintana-Murci, A Call for Blood-In Human Immunology. *Immunity* **50**, 1335-1336 (2019).
120. A. Olin *et al.*, Stereotypic Immune System Development in Newborn Children. *Cell* **174**, 1277-1292 e1214 (2018).
121. S. Kamdar *et al.*, Perinatal inflammation influences but does not arrest rapid immune development in preterm babies. *Nat Commun* **11**, 1284 (2020).
122. A. H. Lee *et al.*, Dynamic molecular changes during the first week of human life follow a robust developmental trajectory. *Nat Commun* **10**, 1092 (2019).

123. C. Peyssonnaux *et al.*, HIF-1alpha expression regulates the bactericidal capacity of phagocytes. *J Clin Invest* **115**, 1806-1815 (2005).
124. A. A. Thompson *et al.*, Hypoxia-inducible factor 2alpha regulates key neutrophil functions in humans, mice, and zebrafish. *Blood* **123**, 366-376 (2014).
125. M. Keel *et al.*, Interleukin-10 counterregulates proinflammatory cytokine-induced inhibition of neutrophil apoptosis during severe sepsis. *Blood* **90**, 3356-3363 (1997).
126. G. Matute-Bello *et al.*, Neutrophil apoptosis in the acute respiratory distress syndrome. *Am J Respir Crit Care Med* **156**, 1969-1977 (1997).
127. M. Uddin *et al.*, Prosurvival activity for airway neutrophils in severe asthma. *Thorax* **65**, 684-689 (2010).
128. C. D. Garlichs *et al.*, Delay of neutrophil apoptosis in acute coronary syndromes. *J Leukoc Biol* **75**, 828-835 (2004).
129. S. Arandjelovic, K. S. Ravichandran, Phagocytosis of apoptotic cells in homeostasis. *Nat Immunol* **16**, 907-917 (2015).
130. N. R. Aggarwal, L. S. King, F. R. D'Alessio, Diverse macrophage populations mediate acute lung inflammation and resolution. *Am J Physiol Lung Cell Mol Physiol* **306**, L709-725 (2014).
131. J. Xu *et al.*, Soluble PD-L1 improved direct ARDS by reducing monocyte-derived macrophages. *Cell Death Dis* **11**, 934 (2020).
132. J. Schulte-Schrepping *et al.*, Severe COVID-19 Is Marked by a Dysregulated Myeloid Cell Compartment. *Cell* **182**, 1419-1440 e1423 (2020).
133. C. A. Thaiss *et al.*, Transkingdom control of microbiota diurnal oscillations promotes metabolic homeostasis. *Cell* **159**, 514-529 (2014).
134. S. Mendez-Ferrer, D. Lucas, M. Battista, P. S. Frenette, Haematopoietic stem cell release is regulated by circadian oscillations. *Nature* **452**, 442-447 (2008).
135. K. D. Nguyen *et al.*, Circadian gene Bmal1 regulates diurnal oscillations of Ly6C(hi) inflammatory monocytes. *Science* **341**, 1483-1488 (2013).
136. J. M. Adrover *et al.*, A Neutrophil Timer Coordinates Immune Defense and Vascular Protection. *Immunity* **50**, 390-402 e310 (2019).
137. J. Gibbs *et al.*, An epithelial circadian clock controls pulmonary inflammation and glucocorticoid action. *Nat Med* **20**, 919-926 (2014).
138. J. M. Adrover *et al.*, A Neutrophil Timer Coordinates Immune Defense and Vascular Protection. *Immunity* **51**, 966-967 (2019).
139. A. Aroca-Crevillen, J. M. Adrover, A. Hidalgo, Circadian Features of Neutrophil Biology. *Front Immunol* **11**, 576 (2020).
140. C. Scheiermann, J. Gibbs, L. Ince, A. Loudon, Clocking in to immunity. *Nat Rev Immunol* **18**, 423-437 (2018).
141. N. C. Allen *et al.*, Desynchronization of the molecular clock contributes to the heterogeneity of the inflammatory response. *Sci Signal* **12**, (2019).
142. N. A. Bokulich *et al.*, Antibiotics, birth mode, and diet shape microbiome maturation during early life. *Sci Transl Med* **8**, 343ra382 (2016).
143. J. D. Forbes *et al.*, Association of Exposure to Formula in the Hospital and Subsequent Infant Feeding Practices With Gut Microbiota and Risk of Overweight in the First Year of Life. *JAMA Pediatr* **172**, e181161 (2018).
144. A. Ardeshir *et al.*, Breast-fed and bottle-fed infant rhesus macaques develop distinct gut microbiotas and immune systems. *Sci Transl Med* **6**, 252ra120 (2014).
145. C. M. Mitchell *et al.*, Delivery Mode Affects Stability of Early Infant Gut Microbiota. *Cell Rep Med* **1**, 100156 (2020).

146. T. Rognes, T. Flouri, B. Nichols, C. Quince, F. Mahe, VSEARCH: a versatile open source tool for metagenomics. *PeerJ* **4**, e2584 (2016).
147. C. Quast *et al.*, The SILVA ribosomal RNA gene database project: improved data processing and web-based tools. *Nucleic Acids Res* **41**, D590-596 (2013).
148. N. Segata *et al.*, Metagenomic biomarker discovery and explanation. *Genome Biol* **12**, R60 (2011).
149. S. Mandal *et al.*, Analysis of composition of microbiomes: a novel method for studying microbial composition. *Microb Ecol Health Dis* **26**, 27663 (2015).
150. H. Wickham, in *Use R!*,. (Springer International Publishing : Imprint: Springer,, Cham, 2016), pp. 1 online resource (XVI, 260 pages 232 illustrations, 140 illustrations in color.
151. T. Kobayashi, H. Kouzaki, H. Kita, Human eosinophils recognize endogenous danger signal crystalline uric acid and produce proinflammatory cytokines mediated by autocrine ATP. *J Immunol* **184**, 6350-6358 (2010).
152. E. A. K. DePasquale *et al.*, cellHarmony: cell-level matching and holistic comparison of single-cell transcriptomes. *Nucleic Acids Res* **47**, e138 (2019).
153. Y. Hao *et al.*, Integrated analysis of multimodal single-cell data. *bioRxiv*, (2020).
154. J. Chen, E. E. Bardes, B. J. Aronow, A. G. Jegga, ToppGene Suite for gene list enrichment analysis and candidate gene prioritization. *Nucleic Acids Res* **37**, W305-311 (2009).
155. A. C. Zambon *et al.*, GO-Elite: a flexible solution for pathway and ontology over-representation. *Bioinformatics* **28**, 2209-2210 (2012).
156. S. de Kleijn *et al.*, IFN-gamma-stimulated neutrophils suppress lymphocyte proliferation through expression of PD-L1. *PloS one* **8**, e72249 (2013).
157. J. K. Juss *et al.*, Acute Respiratory Distress Syndrome Neutrophils Have a Distinct Phenotype and Are Resistant to Phosphoinositide 3-Kinase Inhibition. *Am J Respir Crit Care Med* **194**, 961-973 (2016).
158. E. D. Morrell *et al.*, Alveolar Macrophage Transcriptional Programs Are Associated with Outcomes in Acute Respiratory Distress Syndrome. *Am J Respir Crit Care Med* **200**, 732-741 (2019).
159. A. Liberzon *et al.*, The Molecular Signatures Database (MSigDB) hallmark gene set collection. *Cell Syst* **1**, 417-425 (2015).
160. S. Aibar *et al.*, SCENIC: single-cell regulatory network inference and clustering. *Nat Methods* **14**, 1083-1086 (2017).
161. V. A. Huynh-Thu, A. Irrthum, L. Wehenkel, P. Geurts, Inferring regulatory networks from expression data using tree-based methods. *PloS one* **5**, (2010).

ACKNOWLEDGMENTS: We thank the Cincinnati Children's Hospital Research Foundation's DNA Sequencing Core and Flow Cytometry Laboratories (supported by AR47363, DK78392 and DK90971 from National Institutes of Health [NIH]). We are extremely grateful to the staff at the CNPRC, especially P. Sosa, J. Kendrick, and S. Davis for invaluable help in animal care. We thank J. Whitsett, S. Way, A. Jobe, and S. Pasare for their helpful comments.

Funding: H.D. was supported by HD084686, HL155611, ES029234, HL142708 (NIH), and the Francis Family Foundation, C.C. was supported by ES029234 and AG053498 (NIH), W.Z. was supported by HL140178 (NIH), I.L. was supported by HL149366 and AI152100 (NIH), N.S. was supported by CA226802 and HL148865 (NIH), Y.X. and M.G are supported by U01HL134745 and U01HL122642 (NIH), J.W. was supported by HD89939, EB029863, GM128452 and HD89939 (NIH), L.M. was supported by AI138553 and HL142485 (NIH), D.H. was supported by AI157626, AI150554, 143554 and OD27094 (NIH). The CNPRC is supported by P51 OD11107 (NIH).

Author contributions: H.D., J.G., C.C., L.M., and D.H. designed the experiments. I.L. and W.Z. provided tools. J.W. provided the patient-related metadata. N.S., J.S., Y.X, D.Y, M.G, and H.D. analyzed the single-cell and bulk-transcriptomic data. J.G. and H.D analyzed the cytometry data. J.S., S.S., T.W., M.B. and H.D. wrote the manuscript with other input from M.G., Y.X., C.C., I.L., J.W. D.H., and L.M.

Competing interests: Authors declare no conflicts of interest.

Data Availability: Data discussed in this publication have been deposited in NCBI's Gene Expression Omnibus (accession number GSE176408). Processed data can be further explored at the Lung MAP atlas portal at https://research.cchmc.org/pbge/lunggens/lungExternal/Deshmukh_Macaque_2021.html. Requests for additional materials or processed data can be made via email to the corresponding author.

Code Availability: Scripts used for data analysis are available from GitHub at: https://github.com/Deshmukh-Lab/2021_Stevens_Macaque

SUPPLEMENTAL MATERIALS:

Supplemental Figure 1: Antibiotic exposure in the first week of life causes a unique signature in the peripheral blood immune response.

Supplemental Figure 2: Antibiotic exposure for the first week remodels the pulmonary immune response to respiratory pathogens during infancy.

Supplemental Figure 3: Emergence of neutrophils with senescent and hyperinflammatory features marks pulmonary immune response in dysbiotic newborns

Supplemental Figure 4: Interstitial macrophages with dysfunctional features are a hallmark of the remodeled pulmonary immune response in dysbiotic newborns.

Supplemental Fig 5: Ineffective pulmonary T helper cell responses and increase in stressed, inflammatory innate-like lymphocytes in dysbiotic macaques.

Supplemental Figure 6: Global rewiring of immune cell-to-cell communication networks in dysbiotic newborn macaques.

Supplemental Table 1: Study cohorts of rhesus macaque newborns

Supplemental Table 2: Relative abundances of indicated taxa from 16S amplification of fecal samples

Supplemental Table 3: Cytokine measurements recovered from bronchoalveolar lavages (BAL) at indicated times

Supplemental Table 4: Frequencies of peripheral blood immune cells identified by high-parameter CyTOF

Supplemental Table 5: Beta-diversity measured by unweighted Unifrac analysis of fecal 16S content

Supplemental Table 6: Differential gene analysis of peripheral blood bulk RNAsequencing between control and dysbiotic newborn rhesus macaques and associated GO-term enrichments

Supplemental Table 7: Clinical scoring of newborn rhesus macaques using the Pediatric Early Warning Score (PEWS)

Supplemental Table 8: Differential gene analysis based on UMAP clustering of all immune cell populations ($CD326^{-}CD31^{-}CD45^{+}$) from the lungs of newborn rhesus macaques

Supplemental Table 9: Differential gene analysis of pseudobulk RNAseq data from lungs of control and dysbiotic newborn rhesus macaques

Supplemental Table 10: Cytokines and indicated cell frequencies from bronchoalveolar lavages of control and dysbiotic newborn rhesus macaques following infection with *Streptococcus pneumoniae*

Supplemental Table 11: Differential gene analysis of single-cell RNAseq (scRNAseq) data from lung neutrophils based on UMAP clustering with associated enriched GO pathways

Supplemental Table 12: Module scoring sets used for analysis of scRNAseq data from lung neutrophils of newborn rhesus macaques, gene list derived from PMID: 24015224

Supplemental Table 13: Differential gene analysis of pseudobulk RNAseq data from pulmonary neutrophils in control vs. dysbiotic newborn rhesus macaques

Supplemental Table 14: Correlation of neutrophil gene score from gene signature of neutrophil cluster 2 and clinical outcomes in pediatric sepsis cohort

Supplemental Table 15: SCENIC regulon analysis of scRNAseq data from lung neutrophil clusters of newborn rhesus macaques

Supplemental Table 16: Differential gene analysis of single-cell RNAseq (scRNAseq) data from alveolar macrophages based on UMAP clustering with associated enriched GO pathways

Supplemental Table 17: Module scoring sets used for analysis of scRNAseq data from alveolar macrophages of newborn rhesus macaques

Supplemental Table 18: Differential gene analysis of pseudobulk RNAseq data from alveolar macrophages of control vs. dysbiotic newborn rhesus macaques with associated enriched GO pathways

Supplemental Table 19: Differential gene analysis of pseudobulk RNAseq data from interstitial macrophages of control vs. dysbiotic newborn rhesus macaques with associated enriched GO pathways

Supplemental Table 20: SCENIC regulon analysis of scRNAseq data from alveolar macrophage clusters of newborn rhesus macaques

Supplemental Table 21: Differential gene analysis of pseudobulk RNAseq data from lung $CD4^+$ T cells of control vs. dysbiotic newborn rhesus macaques with associated enriched GO pathways

Supplemental Table 22: Differential gene analysis of pseudobulk RNAseq data from lung innate-like lymphoid (NK) cells of control vs. dysbiotic newborn rhesus macaques with associated enriched GO terms

Supplemental Table 23: Peak PEW scores and unweighted unifrac distances from pretreatment for FT-recipient newborn rhesus macaques at indicated time points

Supplemental Table 24: Differential gene analysis of pseudobulk RNAseq data from lung neutrophils of control vs. dysbiotic vs. FT-recipient newborn rhesus macaques

Supplemental Table 25: Differential gene analysis of pseudobulk RNAseq data from alveolar macrophages of control vs. dysbiotic vs. FT-recipient newborn rhesus macaques

Supplemental Table 26: Differential gene analysis of pseudobulk RNAseq data from lung $CD4^+$ T cells of control vs. dysbiotic vs. FT-recipient newborn rhesus macaques

Supplemental Table 27: List of antibodies used for high-parameter CyTOF

Supplemental Table 28: scRNA sequencing quality data for each sample as indicated

Figure 1: Antibiotic exposure during first week of life delays microbiota maturation, reconfigures the peripheral immune system, and is associated with clinically severe pneumonia.

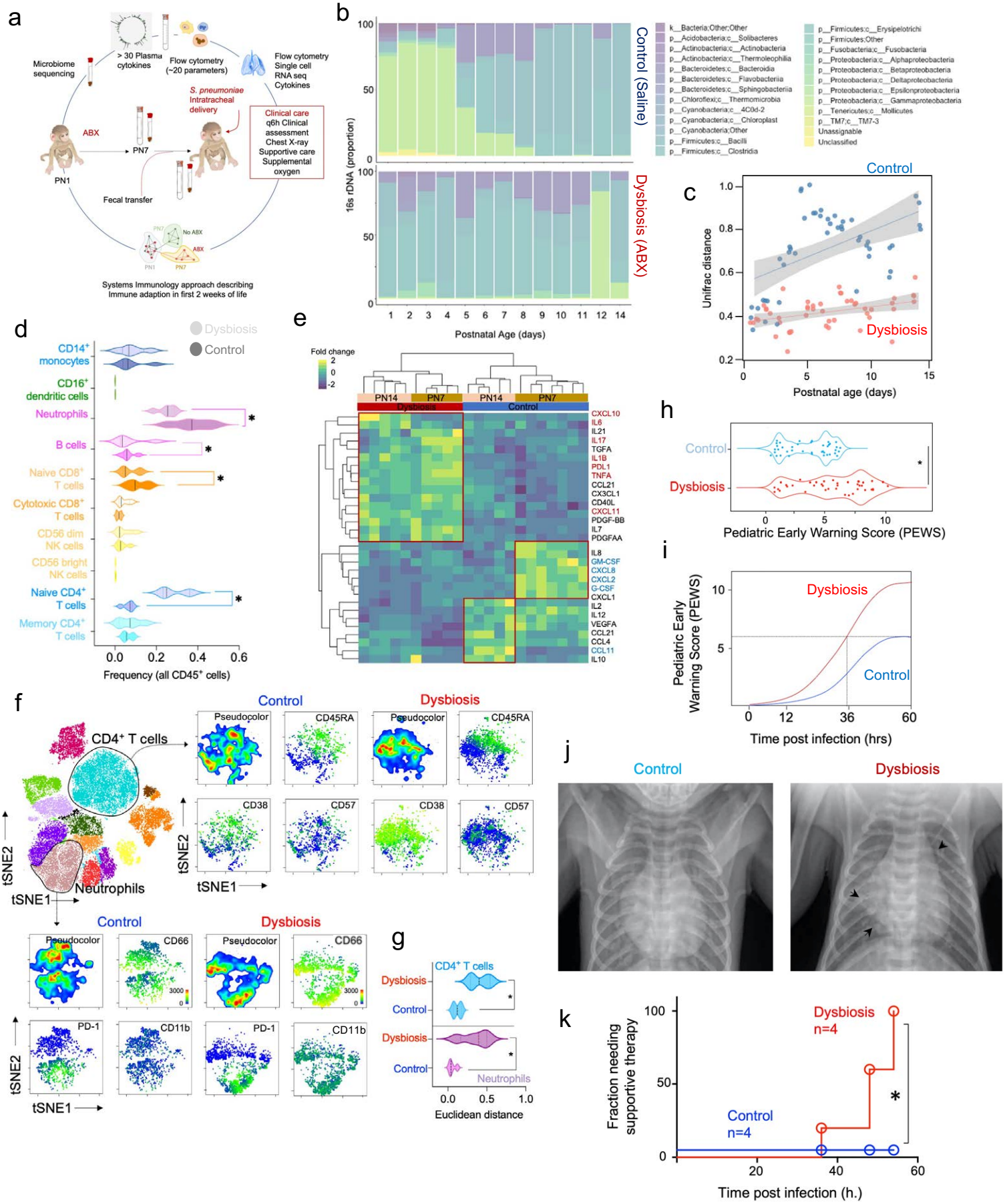

Figure 1: Antibiotic exposure during the first week of life delays microbiota maturation, reconfigures the peripheral immune system, and is associated with clinically severe pneumonia. a) Cohort of vaginally delivered, nursery raised rhesus macaques were treated with a cocktail of antimicrobials from postnatal day (PN) 1 to 7 (Dysbiosis) or with saline (Control) (n = 4 in each experimental group). **b)** Mean relative abundance of fecal bacteria at the genus level at each day of life, for taxa with ≥1% mean relative abundance across all samples in control (top) and dysbiotic (bottom) newborn macaques. **c)** β-diversity (unweighted UniFrac) of fecal bacterial communities at the indicated day of life in control and dysbiotic newborn macaques. Linear fit is shown, and margins represent 95% confidence limits. **d)** Frequencies of the indicated immune cell types in peripheral blood of control and dysbiotic newborn macaques at seven days of life. (n=8, 4 in each experimental group, p-values < 0.05, one-way ANOVA with Tukey's correction for multiple comparisons. Solid lines, median; dotted lines, quartiles). **e)** Abundance of plasma proteins in control and dysbiotic newborn macaques at 7 or 14 days of life, normalized against all subjects and scaled by row. k-means clustering was used to arrange subjects and plasma protein abundance. **f)** Unsupervised analysis of CyTOF cytometry data for $CD4^+$ helper T cells or neutrophils. t-SNE projection of indicated functional markers in $CD4^+$ helper T cells (top) or neutrophils (bottom) in peripheral blood of control and dysbiotic newborn macaques at seven days of life. **g)** Pairwise Euclidean distances between $CD4^+$ helper T cells (top) or neutrophils (bottom) in peripheral blood of control and dysbiotic newborn macaques at seven days of life (n=8, 4 in each experimental group, p-values < 0.05, Student's t-test. Solid lines, median; dotted lines, quartiles). **h)** Peak pediatric early warning score (PEWS) and **i)** progression of PEWS post-infection with *Streptococcus pneumoniae* in control (blue) or dysbiotic (red) newborn macaques. Lines represent the best fit curve by the smoothed spline of the longitudinal distribution of PEWS from the start of infection. Broken lines represent time (post-infection) to PEWS>8, a predetermined threshold to initiate supportive therapy. **j)** Representative chest radiographs obtained at euthanasia in control and dysbiotic newborn macaques. Arrows indicate areas of consolidation. **k)** Kaplan-Meier plot of the fraction of control and dysbiotic newborn macaques requiring supportive therapy at
indicated times post-infection. (n=8, 4 in each experimental group, * p-value < 0.05, Mantel-Cox log-rank test).

Supplemental Figure 1: Antibiotic exposure in the first week of life causes a unique signature in the peripheral blood immune response

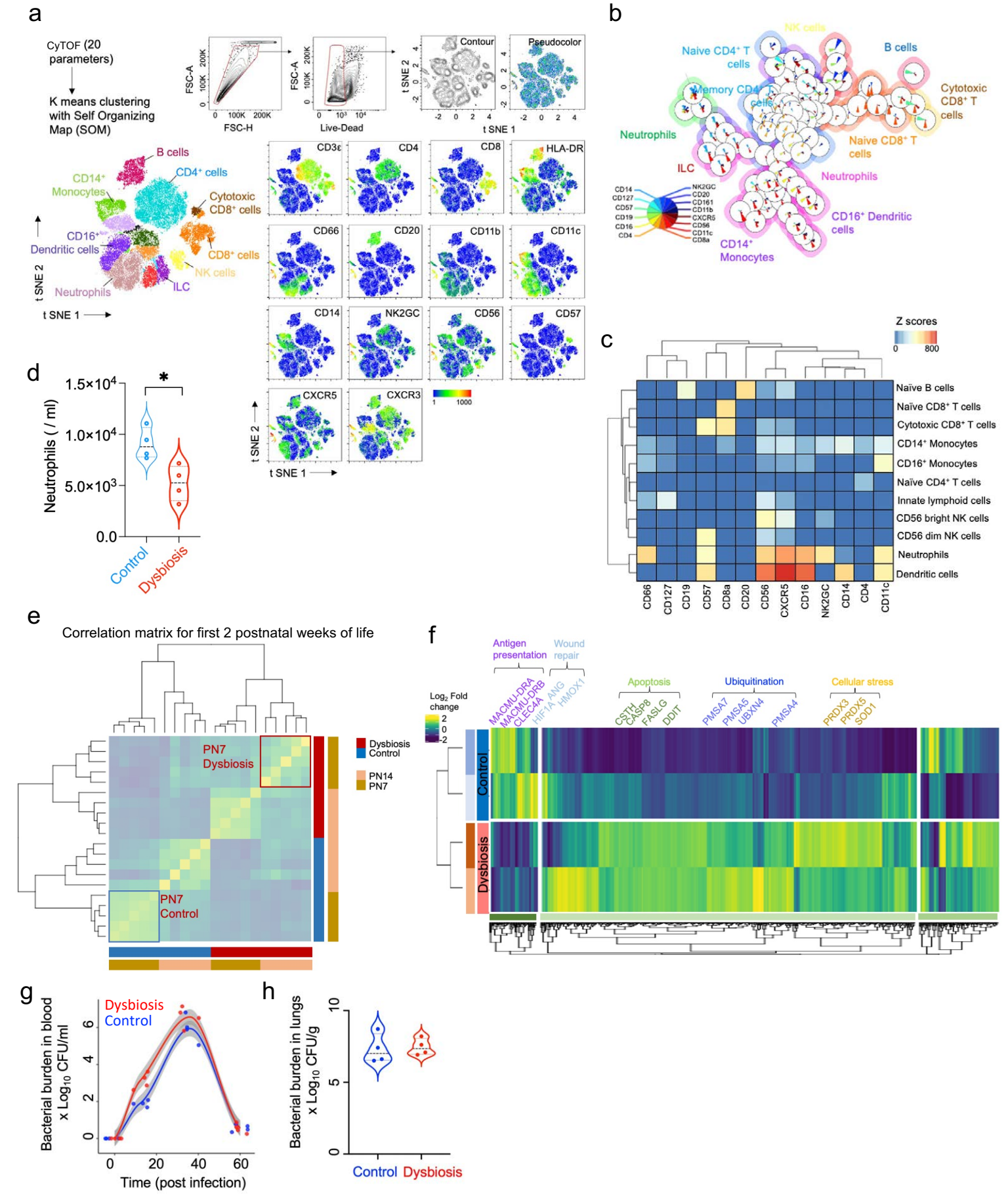

Supplemental Figure 1: Antibiotic exposure in the first week of life causes a unique signature in the peripheral blood immune response. a) Unsupervised analysis of live, single $CD45^+$ cells in the peripheral blood using a self-organizing map (SOM). t-stochastic neighbor embedding (SNE) plot showing expression of key phenotypic markers**.** Immune cells identified by SOM were mapped to tSNE embedding and **b)** organized in a minimal spanning tree (MST). Mean fluorescent intensity (MFI) of key phenotypic surface markers is indicated for each annotated cell type by radial plots. **c)** Row scaled MFI of key phenotypic markers in indicated cell types. k-means clustering of phenotypic markers and cell types. **d)** The absolute number of peripheral blood neutrophils (per mL) in control versus dysbiotic newborn rhesus macaques. Solid lines, median; dotted lines, quartiles. (*, $p < 0.05$). **e)** Pearson's correlation of plasma cytokines with frequencies of indicated immune cells in the peripheral blood of control and dysbiotic subjects. **f)** Row scaled expression of differentially expressed genes in the peripheral blood of control and dysbiotic newborn macaques at seven days of life, normalized against all subjects. k-means clustering was used to arrange subjects and transcripts (n=4, 2 in each experimental group, Benjamini and Hochberg-adjusted p-values < 0.01, $\log_2$ fold change > 2, Wald's test). **g)** Pathogen burden in peripheral blood of control (blue) or dysbiotic (red) newborn macaques at indicated times post-infection with *Streptococcus pneumoniae.* Lines represent the best fit curve by the smoothed spline of the pathogen burden from the start of infection. **h)** Pathogen burden in the lungs of control (blue) or dysbiotic (red) newborn macaques at euthanasia.

Figure 2: Antibiotic exposure for the first week remodels the pulmonary immune response to respiratory pathogens during infancy

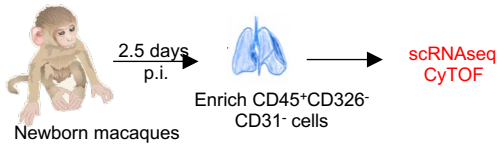

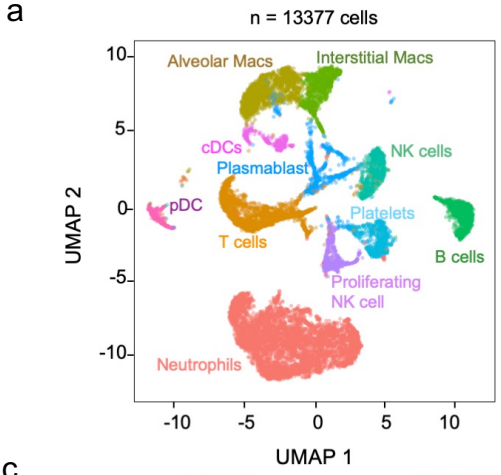

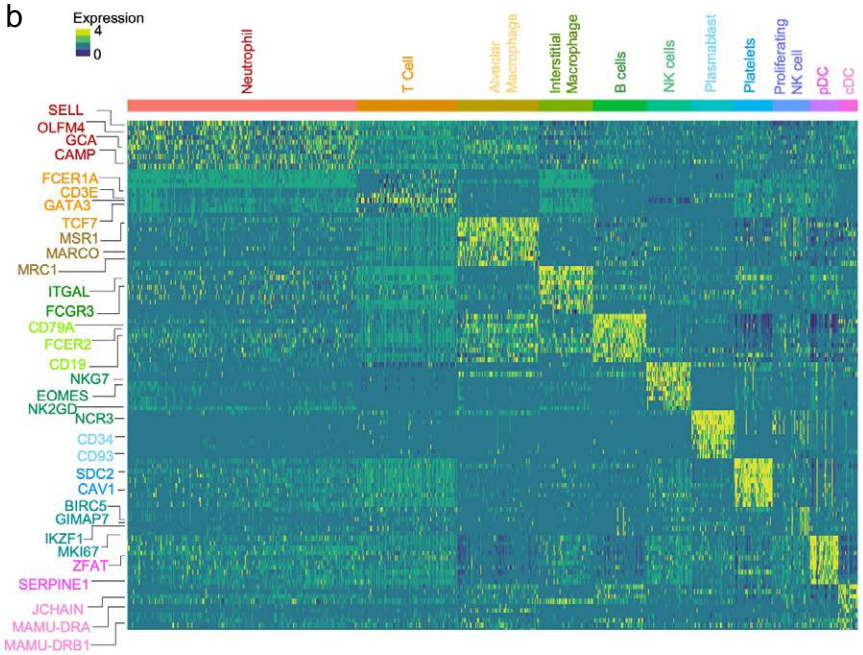

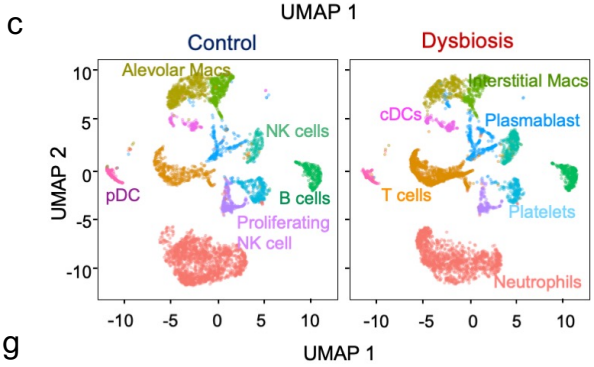

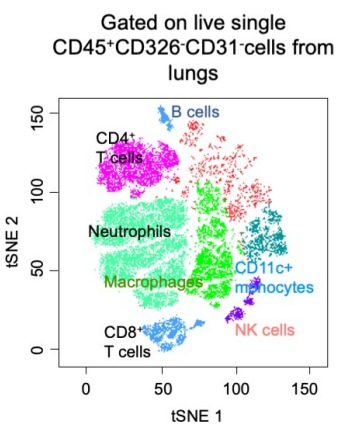

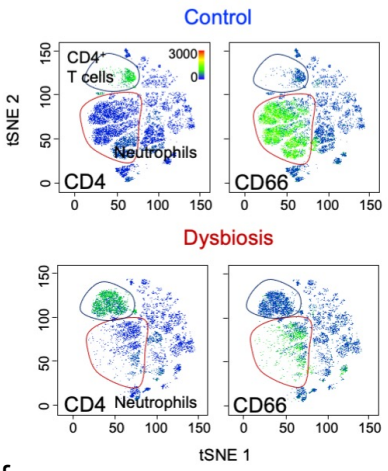

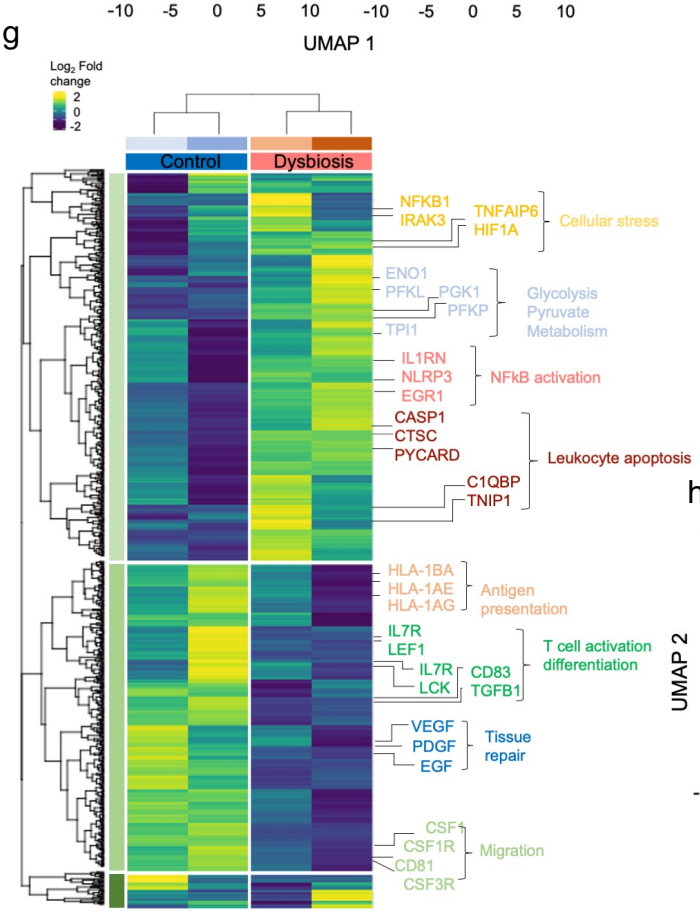

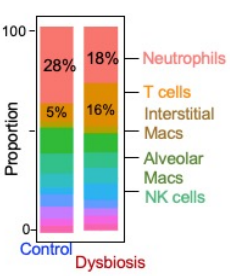

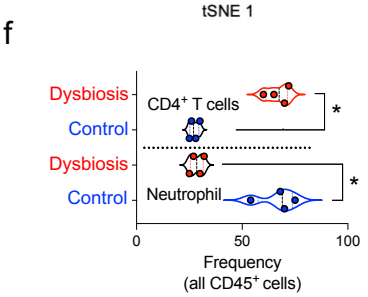

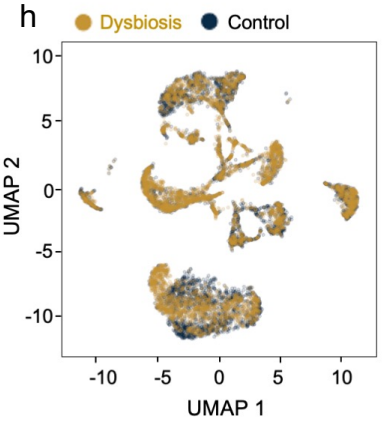

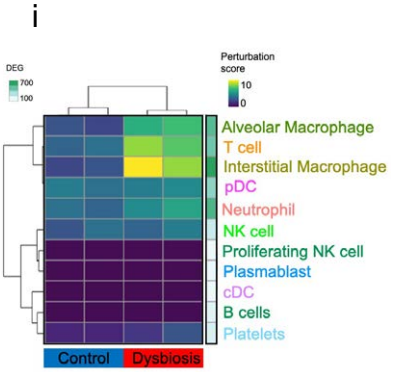

Figure 2: Antibiotic exposure for the first week remodels the pulmonary immune response to respiratory pathogens during infancy. a) Lung from control and dysbiotic newborn macaques (n=4, 2 in each group) was obtained at 60 hrs. post-infection. Lung samples were dissociated into cell suspensions, enriched for immune cells ($EPCAM^-$ $CD31^-CD45^+$), and used for single-cell RNA sequencing (scRNAseq) or CyTOF. Uniform manifold approximation and projection (UMAP) embedding of all samples (n=13377 cells) colored by cell clusters was performed on scRNAseq data of these pulmonary immune cells. **b)** Row scaled expression of the highest differentially expressed genes (DEG) in each cluster (Bonferroni-adjusted p-value < 0.05). **c)** UMAP embedding of lung immune cells and **d)** proportions of each cell type in control and dysbiotic newborn macaques. **e)** CyTOF of lung immune cells. t-SNE embedding of all pulmonary immune cells is shown along with t-SNE embedding of lung neutrophils and $CD4^+$ T cells in control and dysbiotic newborn macaques. **f)** Frequencies of lung $CD4^+$ T cells and neutrophils (of all $CD45^+$ cells from the lungs) (n=8, 4 in each experimental group, p-values < 0.05, Student's t-test, Solid lines, median; dotted lines, quartiles). **g)** Row-scaled expression of differentially expressed genes in the lung immune cells in control and dysbiotic newborn macaques (n=4, 2 in each experimental group), normalized against all subjects. k-means clustering was used to arrange subjects and transcripts (n=4, 2 in each experimental group, Benjamini and Hochberg-adjusted p-values < 0.01, $\log_2$ fold change > 2, Wald's test). **h)** UMAP embedding of all samples (n=15719 cells) colored by treatment (control or dysbiosis) was performed on scRNAseq data of these pulmonary immune cells. **i)** Cellular perturbation scores in indicated samples. The number of differentially enriched genes (DEG) between dysbiotic and control newborn macaques for each cell type is indicated on right.

Supplemental Figure 2: Antibiotic exposure for the first week remodels the pulmonary immune response to respiratory pathogens during infancy

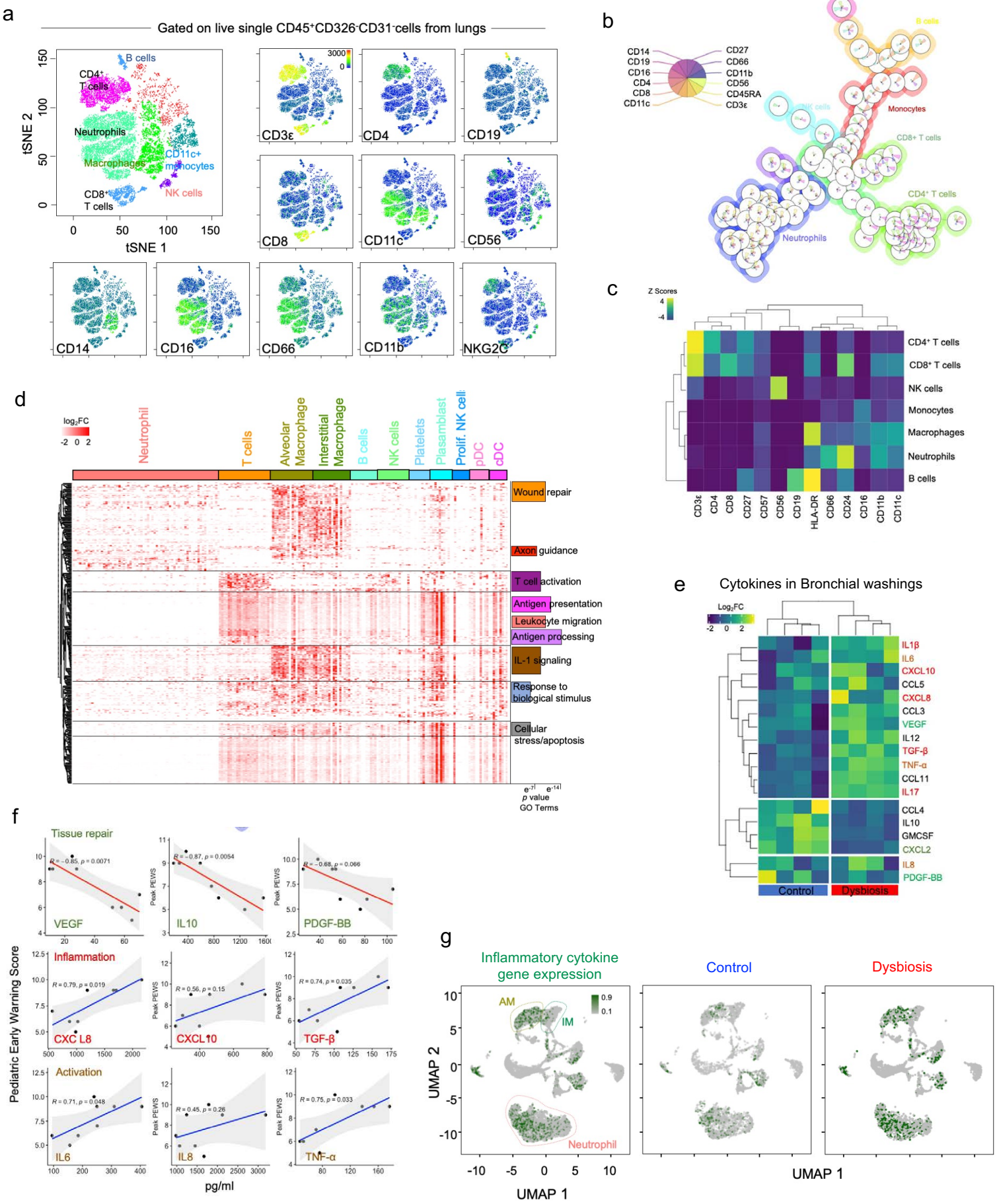

Supplemental Figure 2: Antibiotic exposure for the first week remodels the pulmonary immune response to respiratory pathogens during infancy. a) Unsupervised analysis of live, single immune ($CD45^{+}CD326^{-}CD31^{-}$) cells in the peripheral blood using self-organizing map (SOM). t-stochastic neighbor embedding (SNE) plot showing expression of key phenotypic markers**.** Immune cells identified by SOM were mapped to tSNE embedding and **b)** organized in a minimal spanning tree (MST). **c)** MFI of key phenotypic markers in the indicated cell populations, normalized against all cells and scaled by row. k-means clustering was used to arrange cells and MFI. **d)** Row-scaled expression of the highest differentially expressed genes (DEG) (Bonferroni-adjusted p-value < 0.05) in indicated cell type between control and dysbiotic newborn macaques after infection with *S. pneumoniae*. Bar plot denotes the Benjamini-Hochberg-corrected p-values for Gene Ontology (GO) terms associated with indicated DEG. **e)** Abundance of indicated cytokines in bronchoalveolar washings of both control (blue) and dysbiotic (red) newborn rhesus macaques infected with *S. pneumoniae*, normalized against all subjects and scaled by row. k-means clustering was used to arrange cytokines. **f)** Pearson correlation between amounts of indicated cytokines in the bronchial washings of newborn rhesus macaques infected with *S. pneumoniae* and Pediatric Early Warning Scores (PEWS). Linear fit was assessed with the indicated R values and their associated significance by p-value. **g)** Uniform manifold approximation and projection (UMAP) embedding of all immune cells colored by average expression of inflammatory cytokines. This gene signature was derived from public gene expression datasets (see Methods).

Figure 3: Emergence of neutrophils with senescent and hyperinflammatory features marks pulmonary immune response in dysbiotic newborns

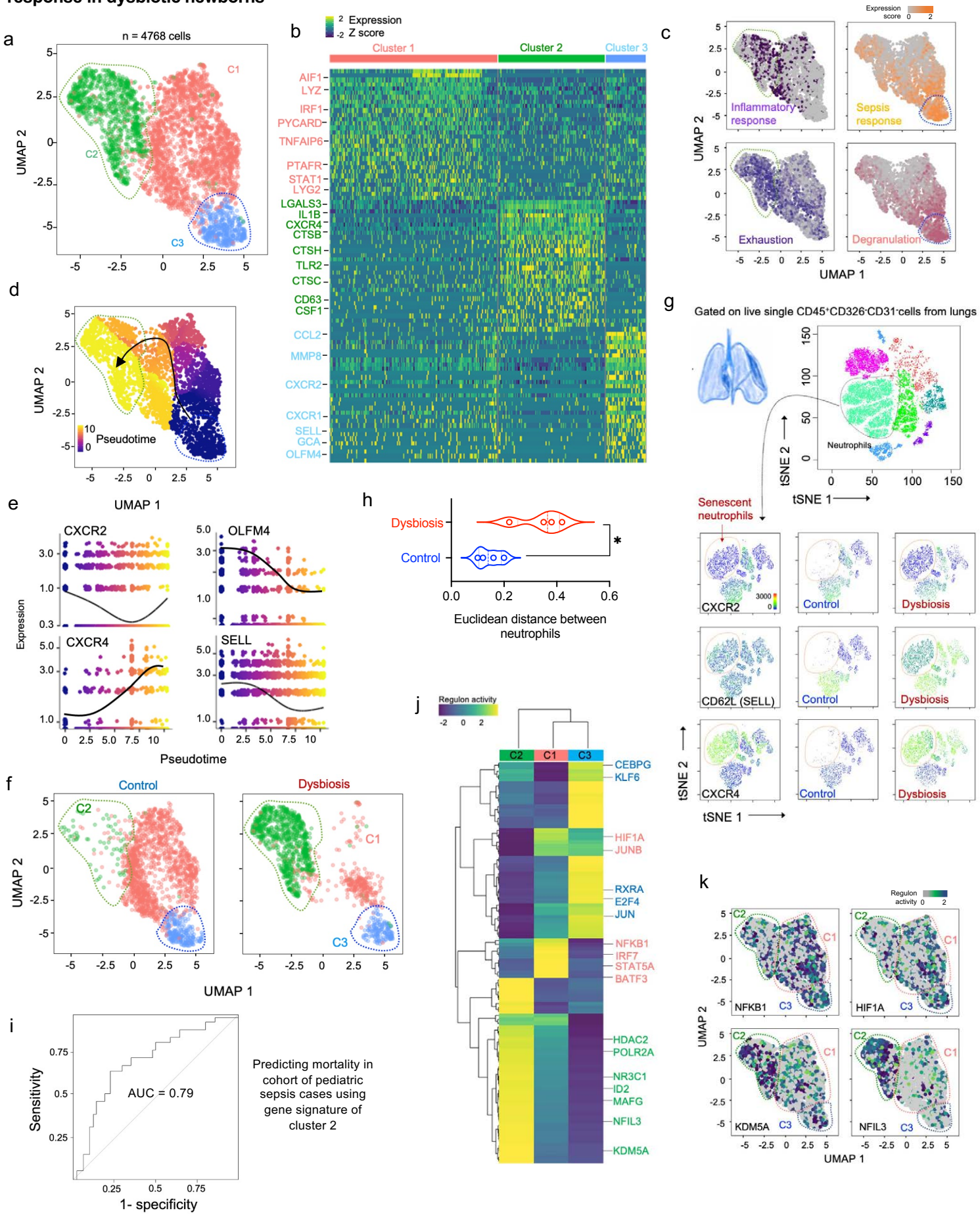

Figure 3: Emergence of neutrophils with senescent and hyperinflammatory features marks pulmonary immune response in dysbiotic newborns. a) Uniform manifold approximation and projection (UMAP) embedding of neutrophils (n= 4768) extracted from a larger dataset of lung immune cells colored by clusters. **b)** Row scaled expression of the highest differentially expressed genes (DEG) in each cluster (Bonferroni-adjusted *p*-values < 0.05). **c)** UMAP embedding of neutrophils colored by average expression of genes associated with inflammatory response (purple), sepsis (orange), exhaustion (blue), and neutrophil degranulation (red). These gene signatures were derived from public gene expression datasets from monocytes in pediatric bacterial sepsis subjects (see Methods). **d)** UMAP embedding of neutrophils colored by pseudotime with overlaid trajectory and **e)** scatter plots showing expression of selected cluster-defining genes across pseudotime. **f)** UMAP embedding of neutrophils colored by cluster in control and dysbiotic newborn macaques. **g)** CyTOF. t-SNE embedding of neutrophils extracted from a larger dataset of lung immune cells (top). Expression of key phenotypic markers (CXCR2, CD62L and CXCR4) is shown (bottom). Neutrophil cluster co-expressing CXCR4 and CD62L is absent in control newborn macaques. **h)** Euclidean distances between neutrophils in lungs of control (bottom) and dysbiotic (top) newborn macaques (n=8, 4 in each experimental group, the *p*-value is indicated, Student's t-test. Solid lines, median; dotted lines, quartiles). **i)** Receiver operating characteristic (ROC) curve depicting sensitivity and specificity of mortality prediction using the gene signature of senescent, hyperinflammatory neutrophils (*HIF1A, CXCR4, CD274, LTF*, and *S100A8*) in an independent cohort of 69 infant sepsis subjects. **j)** Row-scaled regulons activity for neutrophil clusters. k-means clustering was used to arrange clusters and regulons (n=4, 2 in each experimental group, Benjamin and Hochberg-adjusted *p*-values < 0.01). **k)** UMAP embedding of neutrophils colored by regulon activity for indicated regulons, showing that NFIL3 and KDM5A regulons are active in Cluster 2.

Supplemental Figure 3: Emergence of neutrophils with senescent and hyperinflammatory features marks pulmonary immune response in dysbiotic newborns

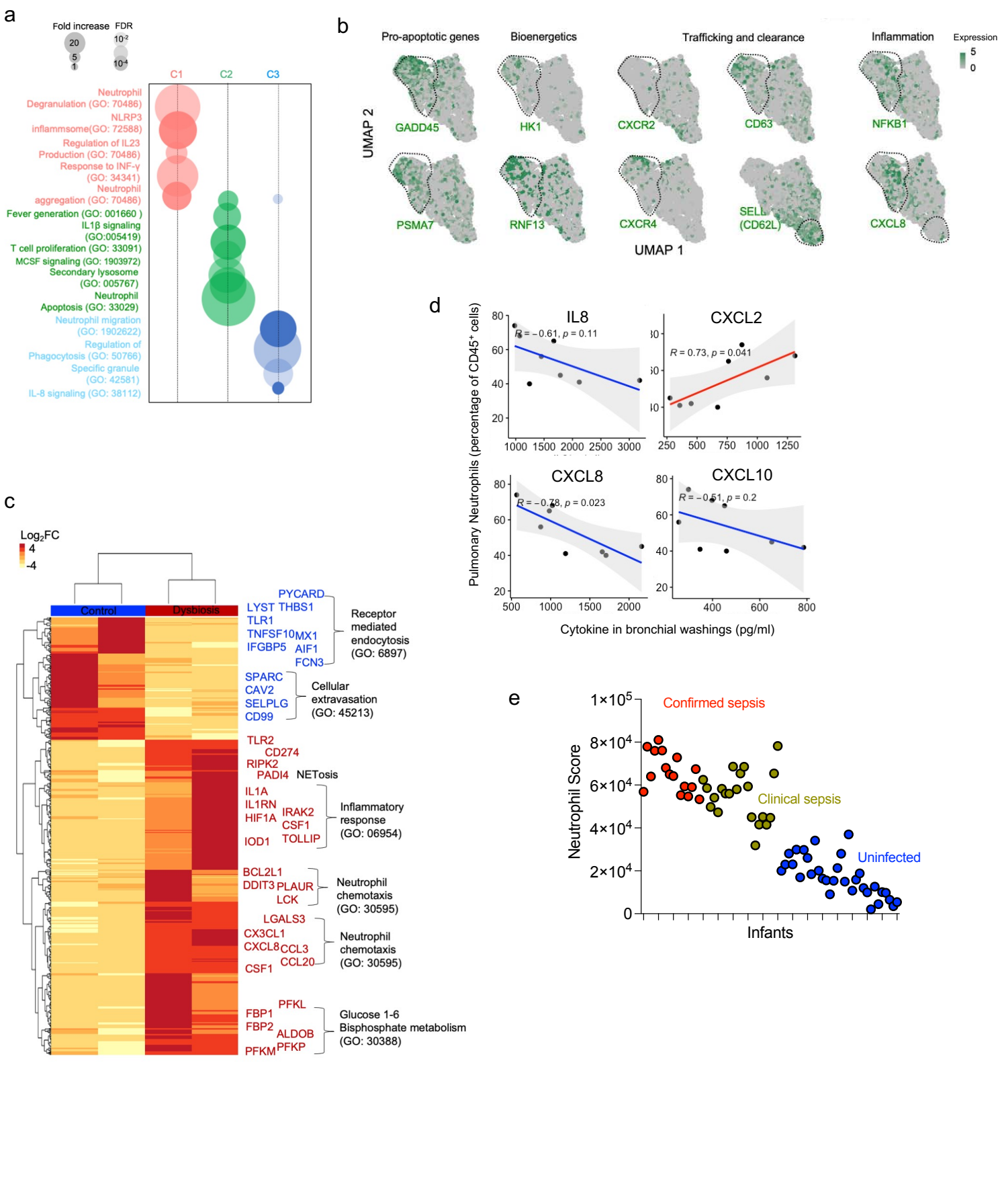

Supplemental Figure 3: Emergence of neutrophils with senescent and hyperinflammatory features marks pulmonary immune response in dysbiotic newborns. a) Selected Gene Ontology (GO) terms associated with differentially enriched genes (DEG) in each cluster (Benjamini-Hochberg-corrected p-values < 0.05 (one-sided Fisher's exact test) are shown and colored by gene ratio. **b)** Expression of genes within the indicated pathways overlaid on the UMAP embedding of neutrophil clusters. **c)** Row scaled expression of DEGs in the pulmonary neutrophils from control (blue) or dysbiotic (red) newborn macaques (n =4, 2 in each experimental group), normalized against all subjects. k-means clustering was used to arrange subjects and transcripts (n=4, 2 in each experimental group, Benjamini and Hochberg-adjusted p-values < 0.01, $\log_2$ fold change > 2, Wald's test). **d)** Pearson correlation between indicated cytokines from bronchial washings (pg/ml) and the frequency of neutrophils (% of $CD45^+$ cells from lungs). Linear fit was assessed with the indicated R values and their associated significance by p-value. **e)** Scatter plot representing the ranked senescent neutrophil signature score (aggregated expression of *HIF1A, CXCR4, CD274, LTF*, and *S100A8,* see Methods) for each infant sample in bulk transcriptomic dataset (see Methods), colored by clinical diagnosis.

Figure 4: Alveolar macrophages with dysfunctional features are a hallmark of the remodeled pulmonary immune response in dysbiotic newborns.

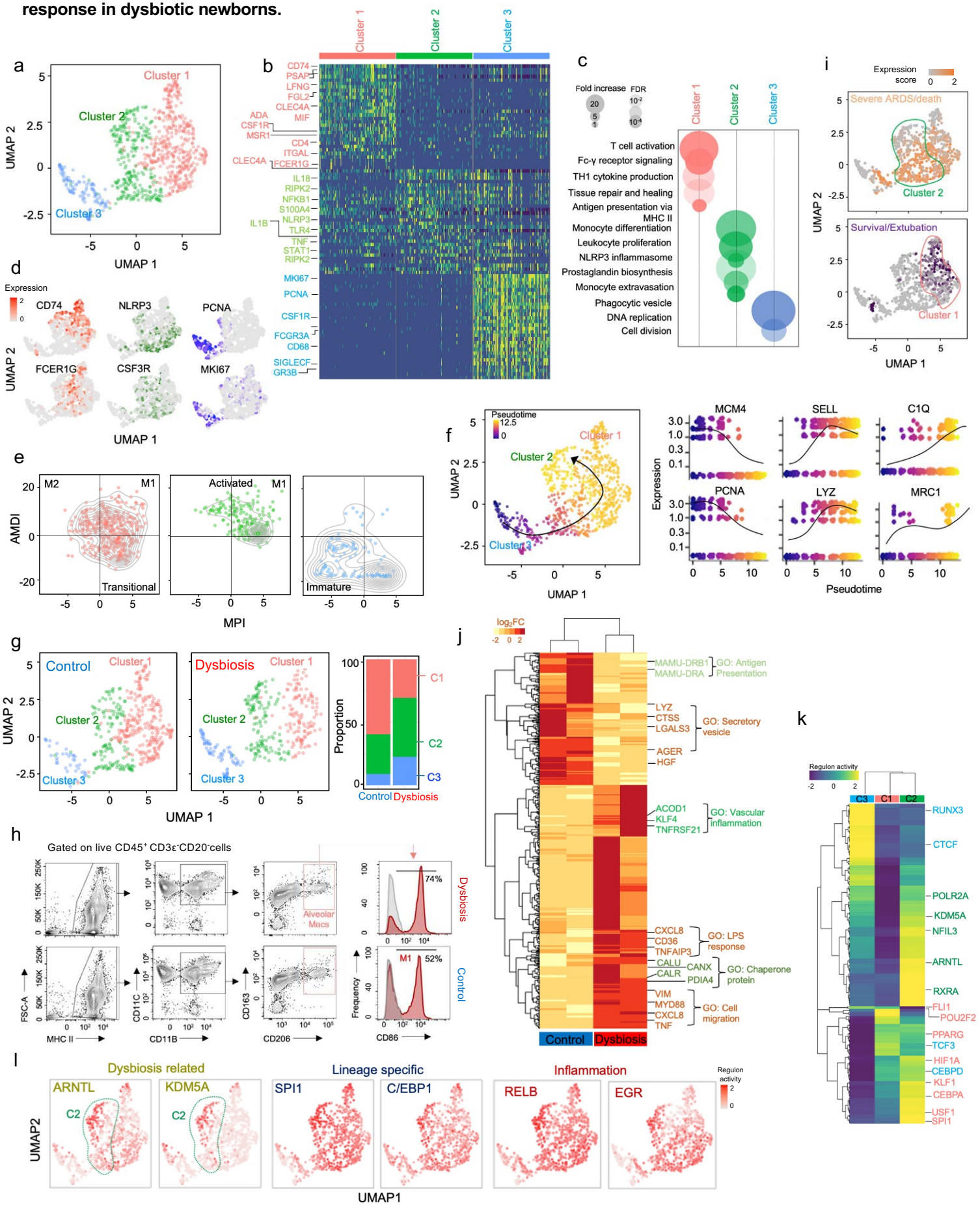

Figure 4: Alveolar macrophages with dysfunctional features are a hallmark of the remodeled pulmonary immune response in dysbiotic newborns. a) Uniform manifold approximation and projection (UMAP) embedding of alveolar macrophages extracted from a larger dataset of lung immune cells colored by clusters. **b)** Row-scaled expression of the highest differentially expressed genes (DEG) in each cluster (Bonferroni-adjusted p-values < 0.05). **c)** Selected Gene Ontology (GO) terms associated with DEG in each cluster (Benjamini-Hochberg-corrected p-values < 0.05 (one-sided Fisher's exact test) are shown and colored by gene ratio. **d)** UMAP embedding of alveolar macrophages colored by expression of selected cluster-specific marker genes. **e)** Scatter plot showing macrophage polarization index (MPI) or activation-induced macrophage differentiation index (AMDI) for each alveolar macrophage, colored by clusters. Cluster 3 represents immature macrophages, cluster 1 represents mature but inactivated macrophages, and cluster 2 represents mature, activated macrophages. **f**) UMAP embedding of alveolar macrophages colored by pseudotime with overlaid trajectory (left) and scatter plots showing expression of selected cluster-defining genes across pseudotime (right). **g**) UMAP embedding of alveolar macrophages colored by cluster (left) and proportions of each cluster in control and dysbiotic newborn macaques (right). **h)** CyTOF. Bivariate contour plots showing gating strategy to identify macrophage subsets and histograms showing co-expression of activation markers, CD86 and CD206, on alveolar macrophages from dysbiotic (top panel) and control (bottom panel) newborn macaques. Numbers indicate the relative frequencies of M1 activated macrophage subset. (n=8, 4 in each experimental group). **i)** UMAP embedding of alveolar macrophages colored by average expression of genes associated with severe ARDS/death (orange) and survival/extubation (purple). These gene signatures were derived from public gene expression datasets from monocytes in pediatric bacterial sepsis subjects (see Methods). **j**) Row-scaled expression of differentially expressed genes in alveolar macrophages from control and dysbiotic newborn macaques (n=4, 2 in each experimental group), normalized against all subjects. k-means clustering was used to arrange subjects and transcripts (n=4, 2 in each experimental group, Benjamini and Hochberg-adjusted p-values < 0.01, $\log_2$ fold change > 2, Wald's test). **k)** Row-scaled regulons activity for alveolar macrophage clusters. k-means clustering was used to arrange clusters and regulons (n=4, 2 in each experimental group, Benjamin and Hochberg-adjusted p-values < 0.01). **l)** UMAP embedding of alveolar macrophages colored by regulon activity associated with dysbiosis (yellow), macrophage lineage specification (blue), and inflammatory response (red).

Supplemental Figure 4: Interstitial macrophages with dysfunctional features are a hallmark of the remodeled pulmonary immune response in dysbiotic newborns.

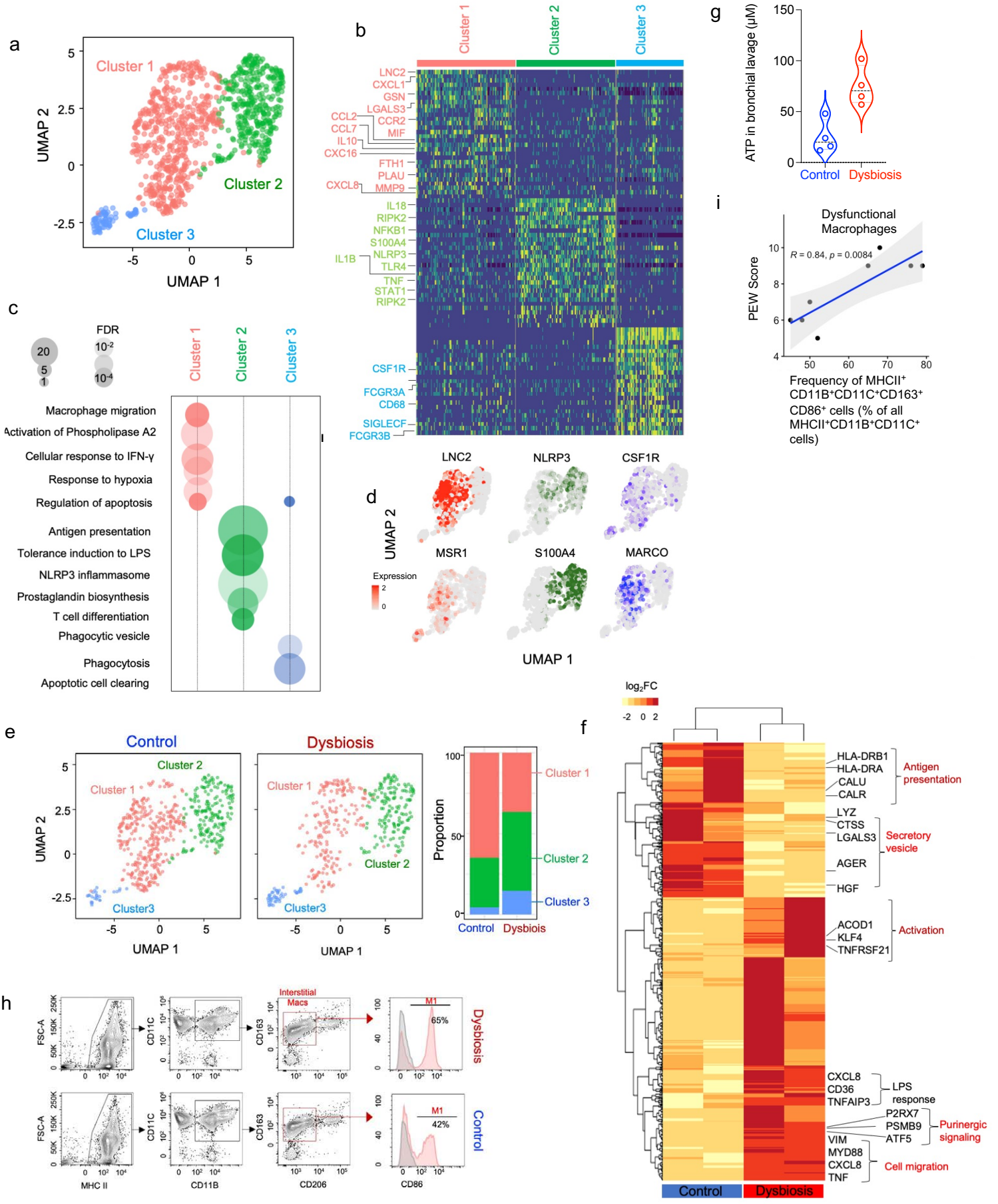

Supplemental Figure 4: Interstitial macrophages with dysfunctional features are a hallmark of the remodeled pulmonary immune response in dysbiotic newborns. a) Uniform manifold approximation and projection (UMAP) embedding of interstitial macrophages extracted from a larger dataset of lung immune cells colored by clusters. **b)** Row scaled expression of the highest differentially expressed genes (DEG) in each cluster (Bonferroni-adjusted p-values < 0.05). **c)** Selected Gene Ontology (GO) terms associated with DEG in each cluster (Benjamini-Hochberg-corrected p-values < 0.05 (one-sided Fisher's exact test) are shown and colored by gene ratio. **d)** UMAP embedding of interstitial macrophages colored by expression of selected cluster-specific marker genes colored by clusters. **e)** UMAP embedding of interstitial macrophages colored by cluster (left) and proportions of each cluster in control and dysbiotic newborn macaques (right). **f)** Row-scaled expression of differentially expressed genes in the interstitial macrophages from control and dysbiotic newborn macaques (n =4, 2 in each experimental group), normalized against all subjects. k-means clustering was used to arrange subjects and transcripts (n=4, 2 in each experimental group, Benjamini and Hochberg-adjusted p-values < 0.01, $\log_2$ fold change > 2, Wald's test). Select GO pathways are labeled to the right of genes. **g)** ATP (uM) measured from bronchial washings of control (blue) and dysbiotic (red) newborn rhesus macaques. Mean, upper, and lower quartiles are indicated. **h)** CyTOF. Bivariate contour plots showing gating strategy to identify macrophage subsets and histograms showing co-expression of activation marker, CD86, on interstitial macrophages from dysbiotic (top panel) and control (bottom panel) newborn macaques. Numbers indicate the relative frequencies of M1 activated macrophage subset. (n=8, 4 in each experimental group). **I**) Pearson correlation of Pediatric Early Warning (PEW) score and the frequency of these activated M1 macrophages as a percent of total macrophages. Correlation coefficient (R) and significance with the associated p-value is indicated.

Figure 5: Changes in communication circuits between neutrophils and macrophages underlie a dysfunctional remodeling of the pulmonary myeloid compartment.

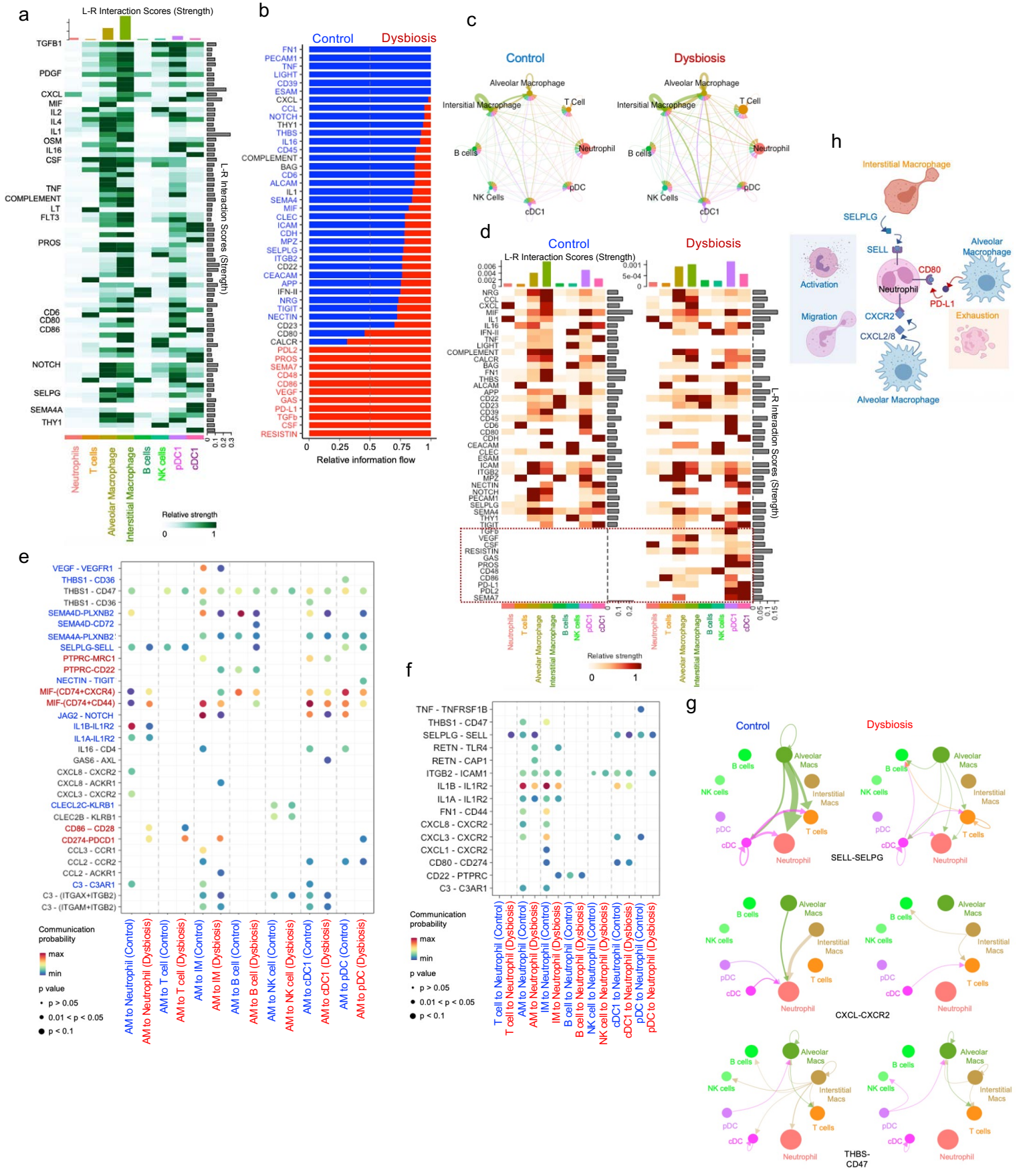

Figure 5: Changes in communication circuits between neutrophils and macrophages underlie a dysfunctional remodeling of the pulmonary myeloid compartment. a) Cell-cell communication network between different pulmonary immune cells. Bar graphs at the top indicate ligand-receptor interaction scores (strength) for each indicated cell type. Bar graphs on the right show the ligand-receptor interaction scores (strength) of each ligand-receptor interaction. The network is dominated by pathways related to inflammation, chemotaxis, and tissue repair, as indicated by selected signal transcripts (on left). **b)** Cell-cell communication pathways ranked by overall information flow in control or dysbiotic newborn macaques. Cell-cell communications enriched in control exposed newborn macaques (in blue text) are dominated by pathways related to tissue homeostasis. Pathways related to chemotaxis (in black text) are equally enriched in control or dysbiotic newborn macaques. Cell-cell communications increased in dysbiotic newborn macaques (in red text) are dominated by pathways related to inflammation. **c**) Circle plot showing differential number of interactions in the cell-cell communication network between control (left) and dysbiotic (right) newborn macaques. Macrophages and Dendritic cells are the hubs (senders), whereas neutrophils and T cells are targets (receivers) of cell-cell communication networks. **d**) Communication pathways related to cell exhaustion and cell activation (boxed) are abundant in dysbiotic compared to control macaques. Bar graphs at the top indicate ligand-receptor interaction scores (strength) for each indicated cell type. Bar graphs on the right show the ligand-receptor interaction scores (strength) of each ligand-receptor interaction. **e**) Dot plot of outgoing signaling patterns from alveolar macrophage (sender) to other immune cells in control (blue) or dysbiotic macaques (red). Dot color reflects communication probabilities and dot size represents computed *p*-values. Empty space means the communication probability is zero. (*p*-values calculated from one-sided permutation test). **f**) Dot plot of incoming signaling patterns to neutrophils (receiver) from other immune cells in control (blue) or dysbiotic macaques (red). (*p*-values computed from one-sided permutation test). **g)** Autocrine and paracrine signaling pathways related to neutrophil migration (CXCL-CXCR2 and THBS1-CD47) and neutrophil activation (SELPLG-SELL) in control or dysbiotic macaques. Circle sizes are proportional to the number of cells in each cell group, and edge width represents the strength of cell-cell communication. **h)** Remodeling of the pulmonary neutrophil compartment may be driven by activating signals received through CXCL-CXCR2, THBS1-CD47 and SELPLG-SELL pathways and lack of inhibitory signaling through the CD80-CD274 pathway (model).

Supplemental Fig 5: Ineffective pulmonary T helper cell responses and increase in stressed, inflammatory innate-like lymphocytes in dysbiotic macaques.

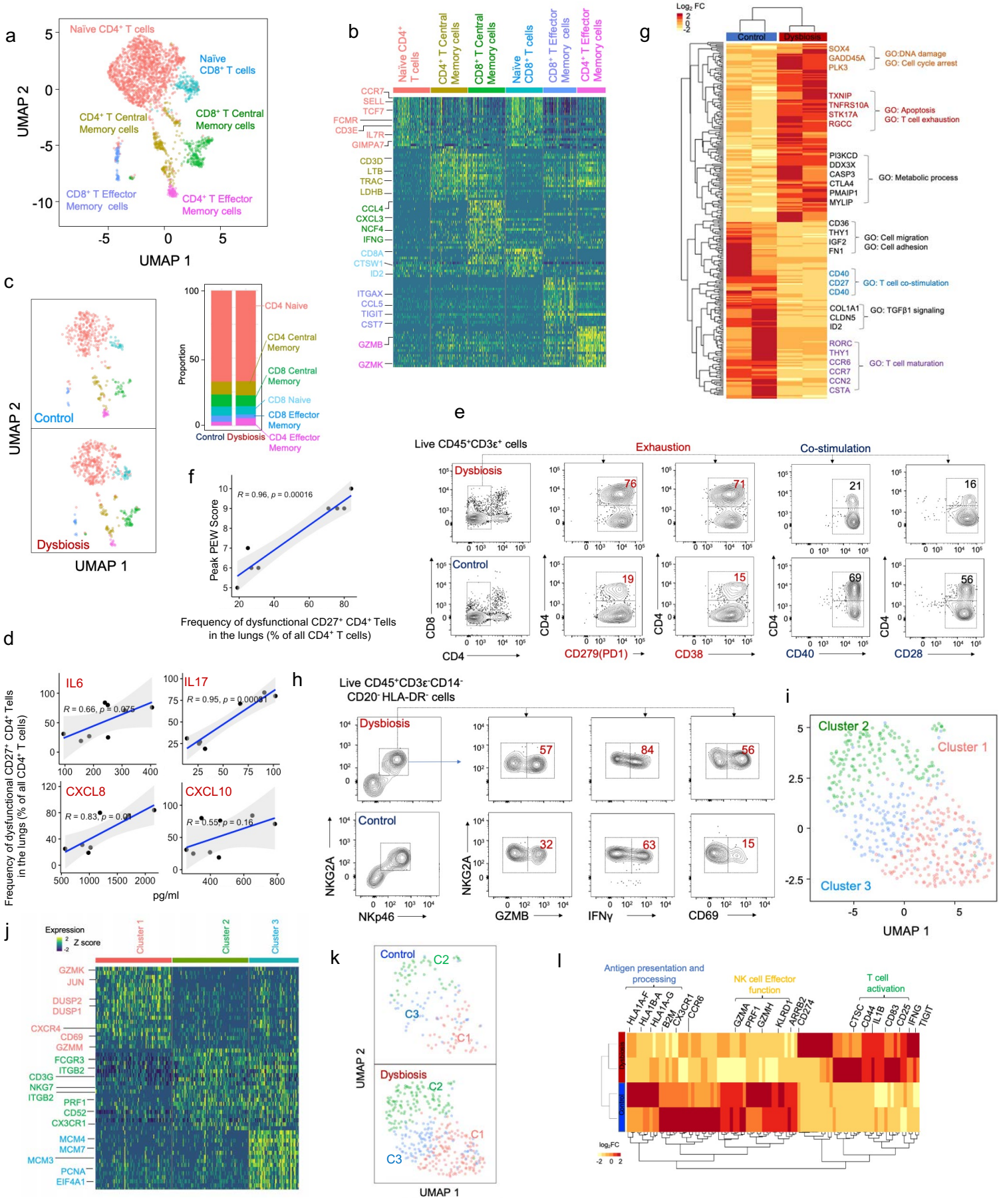

Supplemental Fig 5: Ineffective pulmonary T helper cell responses and increase in stressed, inflammatory innate-like lymphocytes in dysbiotic macaques. a) Uniform manifold approximation and projection (UMAP) embedding of T cells extracted from a larger dataset of lung immune cells colored by cell type labels transferred from publicly available scRNAseq datasets using Seurat v4.0. **b)** Row scaled expression of the highest differentially expressed genes (DEG) in each cluster (Bonferroni-adjusted p-values < 0.05). **c**) UMAP embedding of pulmonary T cells colored by cluster (left) and proportions of each cluster in control and dysbiotic newborn macaques (right). **d**) Pearson correlation between indicated cytokines from bronchial washings (pg/ml) and the frequency of dysfunctional $CD27^+CD4^+$ T cells (% of all CD4+ T cells from lungs). Correlation coefficient (R^2) and significance with the associated p-value is indicated. **e)** Bivariate contour plots showing co-expression of exhaustion markers (CD279[PD1] and CD38) or co-stimulation markers (CD28 or CD40) on $CD4^+$ T helper cells (identified as live $CD45^+$, $CD3\varepsilon^+$, $CD4^+$ cells). Numbers indicate the relative frequencies (n=8, 4 in each experimental group). **f)** Pearson correlation between peak Pediatric Early Warning (PEW) score and the frequency of dysfunctional $CD27^+CD4^+$ T cells (% of all $CD4^+$ T cells from lungs). Correlation coefficient (R) and significance with the associated p-value is indicated. **g)** Row-scaled expression of differentially expressed genes in the pulmonary T cells from control and dysbiotic newborn macaques (n =4, 2 in each experimental group), normalized against all subjects. k-means clustering was used to arrange subjects and transcripts (n=4, 2 in each experimental group, Benjamini and Hochberg-adjusted p-values < 0.01, $\log_2$ fold change > 2, Wald's test). **h)** Bivariate contour plots showing co-expression of CD69 (activation), Granzyme B, or interferon (IFN) γ (cytotoxicity) on pulmonary NK cells (identified as live $CD45^+$ $CD3\varepsilon^-CD14^-CD20^-$HLA-$DR^-$ $NKG2A^+NKP46^+$ cells). Numbers indicate the relative frequencies (n=8, 4 in each experimental group). **i**) UMAP embedding of natural killer (NK) cells extracted from a larger dataset of lung immune cells colored by cluster. **j**) Row scaled expression of the highest differentially expressed genes (DEG) in each cluster (Bonferroni-adjusted p-values < 0.05). **k**) UMAP embedding of NK cells colored by cluster in control and dysbiotic newborn macaques. **l**) Row-scaled expression of differentially expressed genes in the pulmonary NK cells from control and dysbiotic newborn macaques (n =4, 2 in each experimental group), normalized against all subjects. k-means clustering was used to arrange subjects and transcripts (n=4, 2 in each experimental group, Benjamini and Hochberg-adjusted p-values < 0.01, $\log_2$ fold change > 2, Wald's test).

Figure 6: Fecal transfer was associated with favorable changes in pulmonary immune cell responses and improved host resistance to pneumonia in dysbiotic macaques.

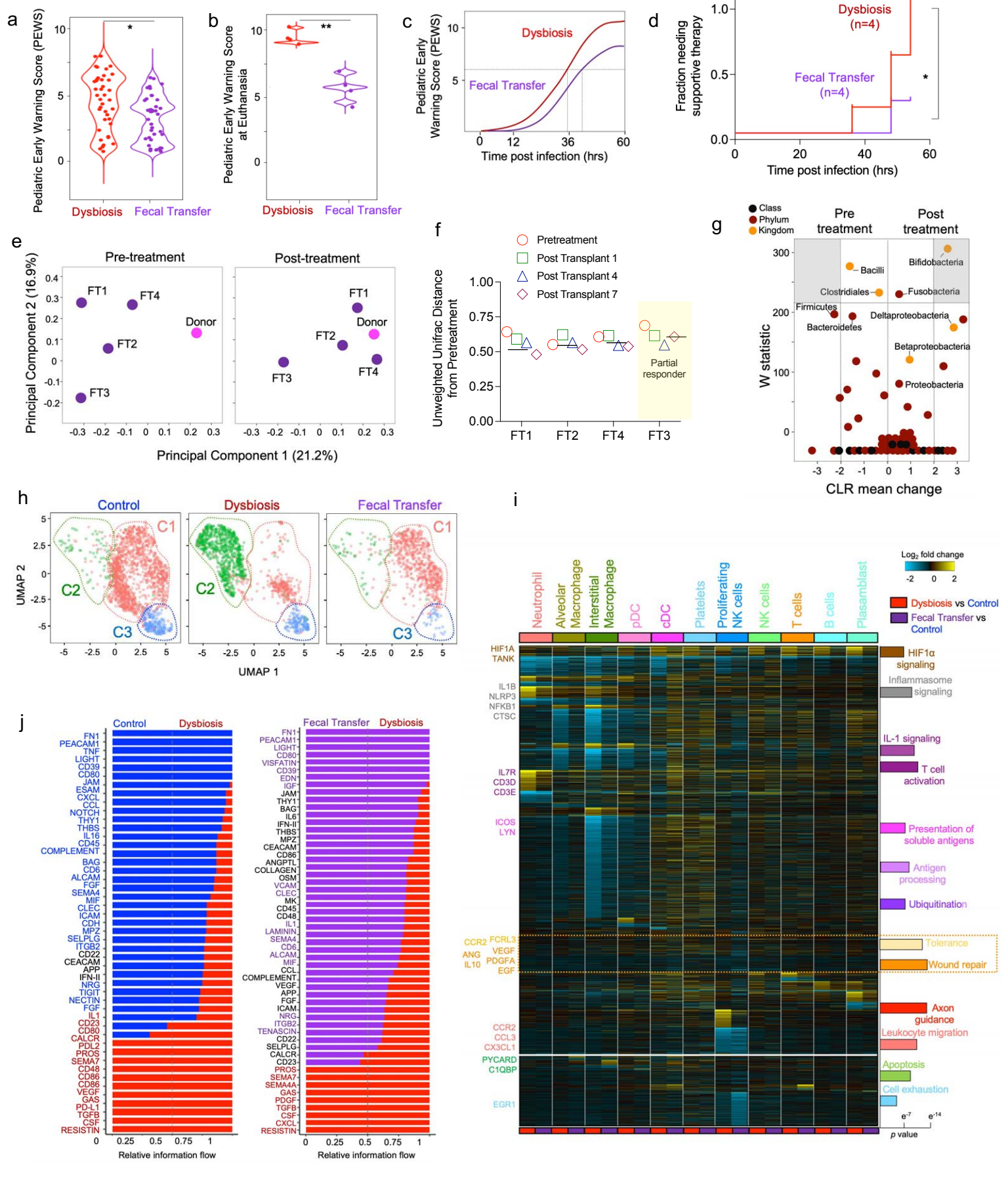

Figure 6: Fecal transfer was associated with favorable changes in pulmonary immune cell responses and improved host resistance to pneumonia in dysbiotic macaques. a) ABX-exposed (Dysbiosis) or Fecal transfer (FT) recipient newborn macaques were challenged with *S. pneumoniae* (serotype 19F) on PN14. Pediatric early warning score (PEWS) was determined every 6 hrs. (n=8, 4 in each experimental group, the *p*-value is indicated, Student's t-test, Solid lines, median; dotted lines, quartiles). Peak PEWS (**a**), **b)** PEWS at euthanasia, and **c)** progression of PEWS post-infection in dysbiotic or FT-recipient newborn macaques. Broken lines (**c**) represent time (post-infection) to PEWS>8, a predetermined threshold to initiate supportive therapy. **d)** Kaplan-Meier plot of the fraction of dysbiotic or FT-recipient newborn macaques requiring supportive therapy at indicated times post-infection. (n=8, 4 in each experimental group, * p <0.05, Mantel-Cox log-rank test). **e)** Principal coordinate analysis (PCA) of fecal bacterial communities of the donor (pink) and the recipients (purple) before (pre-treatment) or seven days after fecal transfer (post-treatment), based on β-diversity (unweighted UniFrac). The distance between samples on the plot represents their dissimilarity. **f)** Dot-plot of Unweighted UniFrac distances for each FT recipient from the corresponding pre-treatment sample at 1-, 4- or 7-days post-transfer. 0 represents identical microbiota compositions, and 1 represents completely dissimilar compositions. The horizontal line represents the average post-treatment distance. **g)** Relative abundance of specific taxa in the recipients before (pre-treatment) or seven days after fecal transfer (post-treatment). Differentially abundant taxa (FDR $q \leq 0.05$, center log transformation >2) are presented in grey margins. The center log transformation (CLR) mean difference represents compositional differences in microbial communities. **h)** Uniform manifold approximation and projection (UMAP) embedding of pulmonary neutrophils colored by cluster in control, dysbiotic, or FT-recipient newborn macaques, showing reappearance of cluster 1. **i)** Heatmap of differentially expressed genes (DEG) in all pairwise cell-type comparisons (fold > 1.2 and eBayes t-test $p < 0.05$, FDR corrected) in dysbiosis or fecal transfer vs. control (cellHarmony). Bar plot denotes the Fisher's Exact *p*-values (FDR corrected) of Gene Ontology (GO) terms adjacent to the enriched cellHarmony DEG cluster. **j)** Cell-cell communication pathways ranked by overall information flow in dysbiotic (red text) or FT-recipient newborn macaques (purple text). Miscommunication in pathways related to inflammation, immune co-stimulation, and cell exhaustion is reversed in FT-recipient newborn macaques. Cell-cell communication associated with tissue repair and cell migration remain uncorrected after FT.

Supplemental Figure 6: Global rewiring of immune cell-to-cell communication networks in dysbiotic newborn macaques.

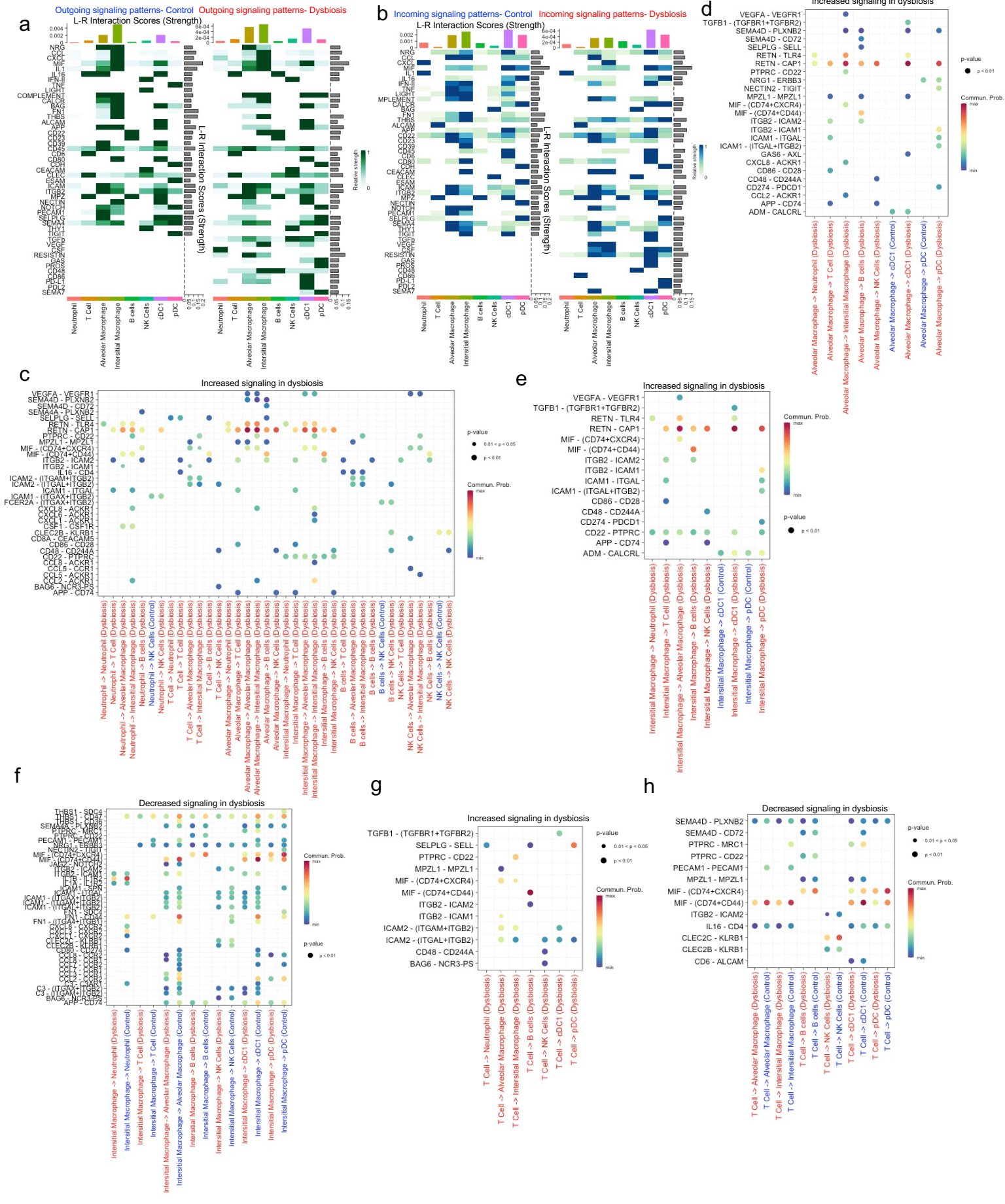

Supplemental Figure 6: Global rewiring of immune cell-to-cell communication networks in dysbiotic newborn macaques.

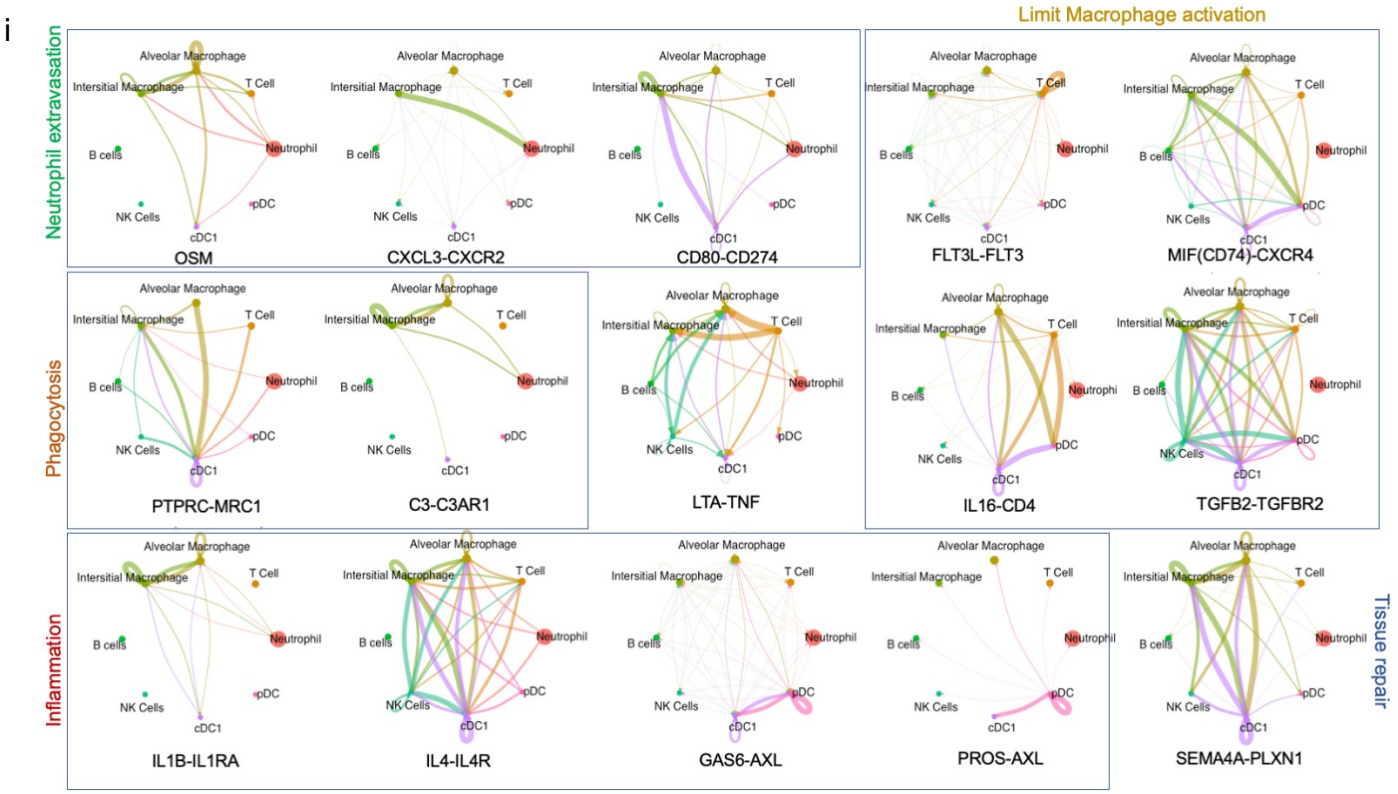

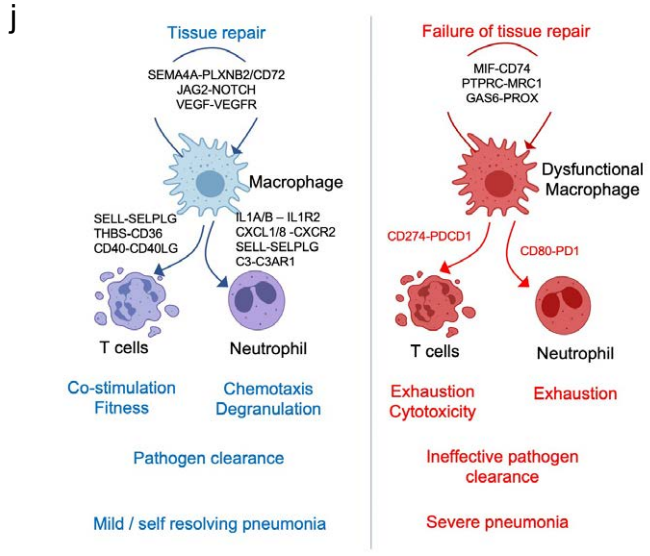

Supplemental Figure 6: Global rewiring of the immune cell-to-cell communication network in dysbiotic newborn macaques. a) Outgoing and **b)** incoming cell-cell communication networks between different pulmonary immune cells in control (left) and dysbiotic (right) newborn rhesus macaques. Bar graphs at the top indicate ligand-receptor interaction scores (strength) for each indicated cell type. Bar graphs on the right show the ligand-receptor interaction scores (strength) of each ligand-receptor interaction. Networks in dysbiotic macaques are dominated by pathways related to inflammation and exhaustion. Networks in control macaques are dominated by tissue repair and regeneration, as indicated by selected signal transcripts (on the left). **c**) Dot plot of signaling patterns increased globally in dysbiotic (red) versus control (blue) macaques. Dot color reflects communication probabilities and dot size represents computed *p*-values. Empty space means the communication probability is zero. (*p*-values calculated from one-sided permutation test). **d**) Dot plot of signaling patterns in alveolar macrophages (senders) increased in dysbiotic (red) versus control (blue) macaques. **e**) Dot plot of signaling patterns in interstitial macrophages (senders) increased in dysbiotic (red) versus control (blue) macaques. **f**) Dot plot of signaling patterns in interstitial macrophages (senders) decreased in dysbiotic (red) versus control (blue) macaques. **g**) Dot plot of signaling patterns in T cells (senders) increased in dysbiotic (red) versus control (blue) macaques. **h**) Dot plot of signaling patterns in T cells (senders) decreased in dysbiotic (red) versus control (blue) macaques. **i)** Autocrine and paracrine signaling pathways related to neutrophil extravasation (OSM, CXCL3-CXCR2 and CD80-CD274[PDL1]), phagocytosis (PTPRC-MRC1, C3-C3AR1), inflammation (IL1B-IL1RA, IL4-IL1R, GAS-AXL, and PROS-AXL), limiting macrophage activation (FLT3L-FLT3, MIF-CD74, and TGFB2-TGBR) and repair (SEMA4A-PLXN1). Circle sizes are proportional to the number of cells in each cell group, and edge width represents the strength of cell-cell communication. **j**) Neutrophils and $CD4^+$ T cells transform the first-order cytokine signals into second-order cytokines that enhance the trafficking and extravasation (OSM-LIFR), immune co-activation (Complement C3-C3AR1), and effector function, such as phagocytosis (PTPRC-MRC1), to eliminate pathogens. Reciprocal interactions limit macrophage activation (MIF-CD74/CXCR2 and CD83-PECAM1) and promote tissue-repair factors (CSF1-CSFR1, TGFBR3-TGFB1, SEMA4-NRP). Sequential engagement of these communication circuits ensures that the minimum necessary response to a microbe is engaged (model).

Supplemental Figure 7: Fecal transfer was associated with favorable changes in pulmonary immune cell responses and improved host resistance to pneumonia in dysbiotic macaques.

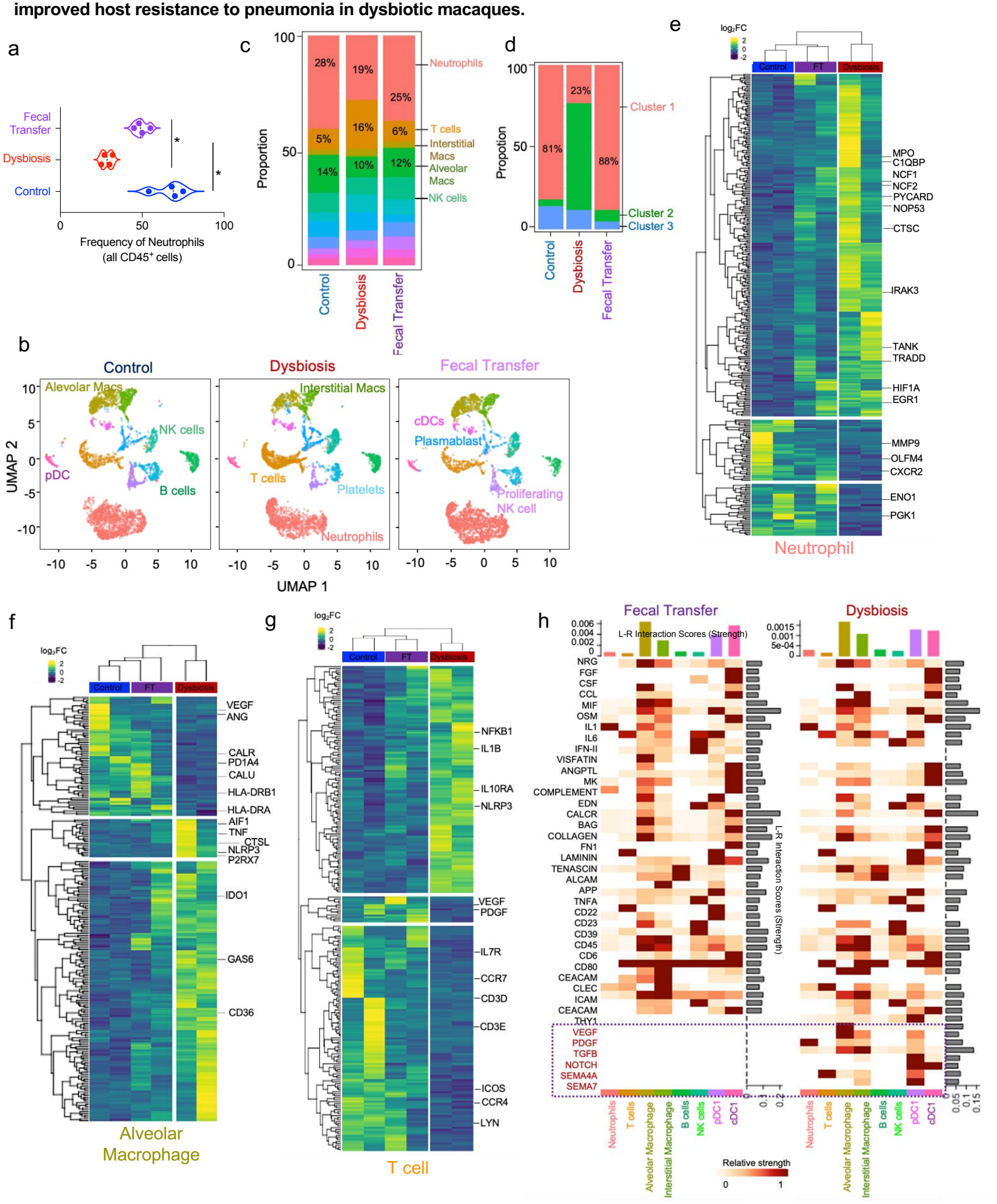

Supplemental Figure 7: Fecal transfer was associated with favorable changes in pulmonary immune cell responses and improved host resistance to pneumonia in dysbiotic macaques. a) Frequency of lung neutrophils (as a percentage of all $CD45^+$ cells from lungs) from control, dysbiotic, and fecal transplant (FT) newborn rhesus macaques. *, $p < 0.05$. **b)** Uniform manifold approximation and projection (UMAP) embedding of pulmonary immune cells colored by cluster in control (left), dysbiotic (middle), or FT-recipient (right) newborn macaques**. c)** Frequencies of indicated lung immune cell populations (as percentage of all $CD45^+$ cells from lungs) from control, dysbiotic, and FT newborn rhesus macaques. **d)** Frequency of lung neutrophil clusters (as percentage of all lung neutrophils) from control, dysbiotic, and FT newborn rhesus macaques. **e)** Row-scaled expression of differentially expressed genes in pulmonary neutrophils or **f)** alveolar macrophages or **g)** pulmonary T cells in control, dysbiotic, or FT-recipient newborn macaques, normalized against all subjects. k-means clustering was used to arrange subjects and transcripts (n=4, 2 in each experimental group, Benjamini and Hochberg-adjusted p-values < 0.01, $\log_2$ fold change > 2, Wald's test). **h**) Strength of cell-cell communication pathways in dysbiotic and FT-recipient newborn macaques. Communication pathways related to tissue repair and chemotaxis (boxed) remain dysregulated despite FT. Bar graphs at the top indicate ligand-receptor interaction scores (strength) for each indicated cell type. Bar graphs on the right show the ligand-receptor interaction scores (strength) of each ligand-receptor interaction.